Economic Geology
Vol. 82, 1987, pp. 600–634

Sulfur and Lead Isotope Studies of Stratiform Zn-Pb-Ag Deposits, Anvil Range, Yukon: Basinal Brine Exhalation and Anoxic Bottom-Water Mixing

WAYNE C. SHANKS III, LAUREL C. WOODRUFF,

U. S. Geological Survey, National Center, Mail Stop 954, Reston, Virginia 22092

GREGG A. JILSON,*

Cyprus-Anvil Mining Corporation, 330–355 Burrard Street, Vancouver, British Columbia, Canada V6C 2G8

DAVID S. JENNINGS,

Northern Dynasty Explorations Ltd., 400 Burrard Street, Vancouver, British Columbia, Canada V6C 2G8

JANET S. MODENE,

Cominco American, 15120 East Euclid, Spokane, Washington 99216

AND BARRY D. RYAN

Crows Nest Resources, P.O. Box 2699, Station M, Calgary, Alberta, Canada T2P 2M7

Abstract

Five stratiform Zn-Pb-Ag deposits are known in Early Cambrian metapelitic rocks along a curvilinear trend in the Anvil Range, central Yukon. The Anvil Range deposits occur along the southwestern boundary of the Selwyn basin in the stratigraphic transition zone between metapelites of the Mt. Mye unit and calcareous phyllites of the overlying Vangorda unit. The massive sulfides are associated closely with anomalously thick graphitic phyllites, apparently related to a second-order basin. A typical Anvil cycle of mineralization begins with a ribbon-banded graphitic-quartzitic-pyritic unit. This grades upward into sulfide-bearing quartzite, quartzitic massive sulfide, massive sulfide, and finally a baritic massive sulfide horizon. Sericitic alteration envelopes irregularly encompass each deposit and locally are developed best in footwall rocks.

Detailed sulfur isotope studies have been carried out on the DY and Grum deposits and on one representative drill hole from the Faro deposit. The $\delta^{34}S$ values of sulfide minerals generally range from 10 to 22 per mil and are similar in all three deposits. The $\delta^{34}S$ values of pyrite in unmineralized samples from the district exhibit a wider range, from 6 to 34 per mil, and show distinct upward stratigraphic increase due to a stagnation cycle in the basin.

The $\delta^{34}S$ values of barite samples are strongly dependent on bottom-water conditions and mode of mixing during brine exhalation. They range from 22 to 26 per mil in the Faro deposit to 36 to 42 per mil in the DY deposit. These variations are due to mixing of isotopically light sulfate (18–20‰) in Ba-bearing ore fluid and isotopically heavy residual sulfate (30–60‰) in anoxic seawater.

Thirty-eight samples of galena from the DY, Grum, Faro, SB, and Swim deposits have been analyzed for lead isotope ratios. In general, the lead isotope ratio data indicate an upper crustal lead source, with the Proterozoic Grit unit which is inferred to underlie the district being the most likely source rock. A small component of mantle leads from mafic igneous rocks or due to source rock inhomogeneity is also indicated.

Graphitic host lithologies, lack of stratiform iron oxides, $\delta^{34}S$ values of sedimentary pyrite, and sulfide sulfur-organic carbon variations in unmineralized cores indicate formation of the Anvil deposits in strongly reduced bottom water related to a previously unknown Early Cambrian anoxic event.

Introduction

THE Anvil lead-zinc-silver district is located 200 km northeast of Whitehorse in the Yukon Territory (Fig. 1). Open-pit mining of the Faro deposit, at up to 10,000 metric tons per day from 1969 until a temporary closure in 1982,[1] constitutes the Yukon Territory's largest mining operation. District-wide total

* Present address: Curragh Resources, 117 Industrial Road, Whitehorse, Yukon, Canada Y1A 2T8.

[1] Note added in proof: Faro mine reopened in 1986, with an average production of 13,500 metric tons per day.

0361-0128/87/666/600-35$2.50

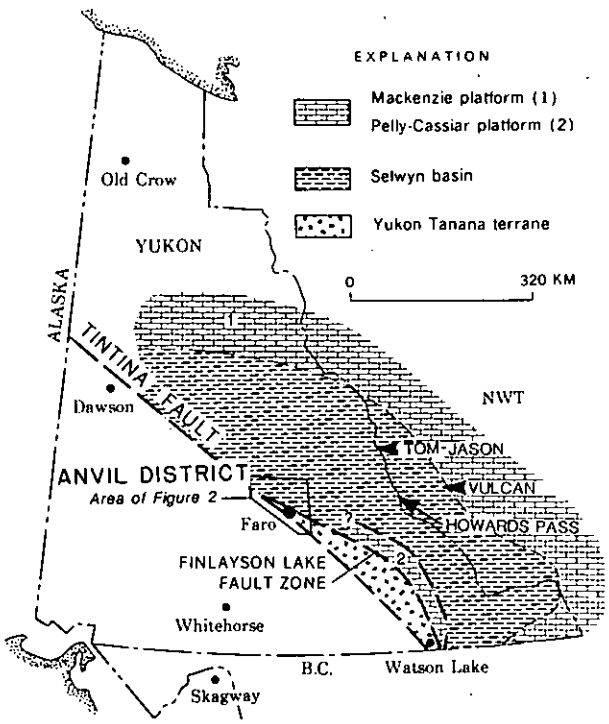

FIG. 1. Location of the Anvil Pb-Zn-Ag district with respect to selected Paleozoic and Mesozoic tectonic elements northeast of the Tintina fault. The Tintina fault is a Late Cretaceous, right-lateral strike-slip fault with approximately 450 km displacement. The Yukon Tanana terrane (also known as the Yukon cataclastic complex) is an imbricated sequence of middle Paleozoic magmatic arc-related rocks and upper Paleozoic ophiolitic rocks; it is exotic with respect to the Yukon farther northeast and was "accreted" in the Late Jurassic or Early Cretaceous along the Finlayson Lake fault zone, a major transcurrent fault or upturned thrust.

sulfide is inferred to be as much as 275 million metric tons containing measured reserves of 92 million metric tons of ore containing 8.3 percent combined lead-zinc with about 50 g/ton silver (Table 1).

Five stratiform pyritic massive sulfide deposits and two lesser occurrences occupy a narrow interval in the late Proterozoic to early Paleozoic section of the Anvil Range (Fig. 2). Detailed sulfur and lead isotope studies were undertaken to define lateral and vertical isotopic variation in the deposits and to shed further light on the origin of the deposits. In particular, $\delta^{34}S$ data for the sedimentary exhalative deposits of the Anvil Range, when compared to temporal seawater sulfate curves, provide information on the ultimate sulfur source. Likewise, lead isotope data provide constraints on the ultimate lead source. Small lateral and vertical variations in $\delta^{34}S$ values of sulfide and sulfate minerals allow refinement of genetic models. Comparative study of unmineralized metapelite host rocks in the Anvil Range, which includes analysis of organic carbon and sulfide sulfur contents, also was undertaken to assess regional bottom water conditions during ore formation.

Previous studies of $\delta^{34}S$ variations in Anvil Range massive sulfide deposits have been carried out by Campbell and Ethier (1974) and by Kuo (1976). However, recent improvements in understanding of facies relationships in Anvil deposits were not available to these authors, thus hampering both sample selection and data interpretation. Lead isotope data on Anvil Range deposits have previously been presented by LeCouter (1973), Kuo and Folinsbee (1974), Kuo (1976), and Godwin and Sinclair (1982). The present interpretations make full use of geologic information now available for the Anvil Range and focus on the sources of lead and sulfur in the deposits.

The detailed sulfur isotope studies of sedimentary pyrite samples in pelitic rocks of the Anvil Range, coupled with the recently published curves of Goodfellow and Jonasson (1984), indicate a remarkable picture of the Selwyn basin as a stagnating, extremely reducing sea for over 200 m.y. of the early Paleozoic. Moreover, the combination of an excellent Pb-Zn-Ba source rock underlying and flanking the basin and of basin-margin block faults, which provide pathways for subsurface brines to vent on the sea floor, has produced an important metallogenic province for stratiform and strata-bound Pb-Zn deposits, which includes the Anvil deposits. If one accepts the inferences of Goodfellow and Jonasson (1984) and this study regarding extensive sulfate reduction in the anoxic water

TABLE 1. Ore Reserves for Anvil District Deposits[1]

Deposit	Measured reserves	Grade			Inferred total sulfide
		Lead (%)	Zinc (%)	Silver (g/t)	
Faro	36.9 m.t.	3.0	4.8	37	70 m.t.
Grum	27.8 m.t.	3.1	4.9	48	50–80 m.t.
Vangorda	5.2 m.t.	3.3	4.3	48	10–15 m.t.
DY	18.0 m.t.	5.6	7.4	83	70–100 m.t.
Swim	4.3 m.t.	4.7	3.8	47	8–10 m.t.
Composite	92.2 m.t.	3.6	4.7	50	208–275 m.t.

[1] 1981 reserve figures, given in million metric tons (m.t.)

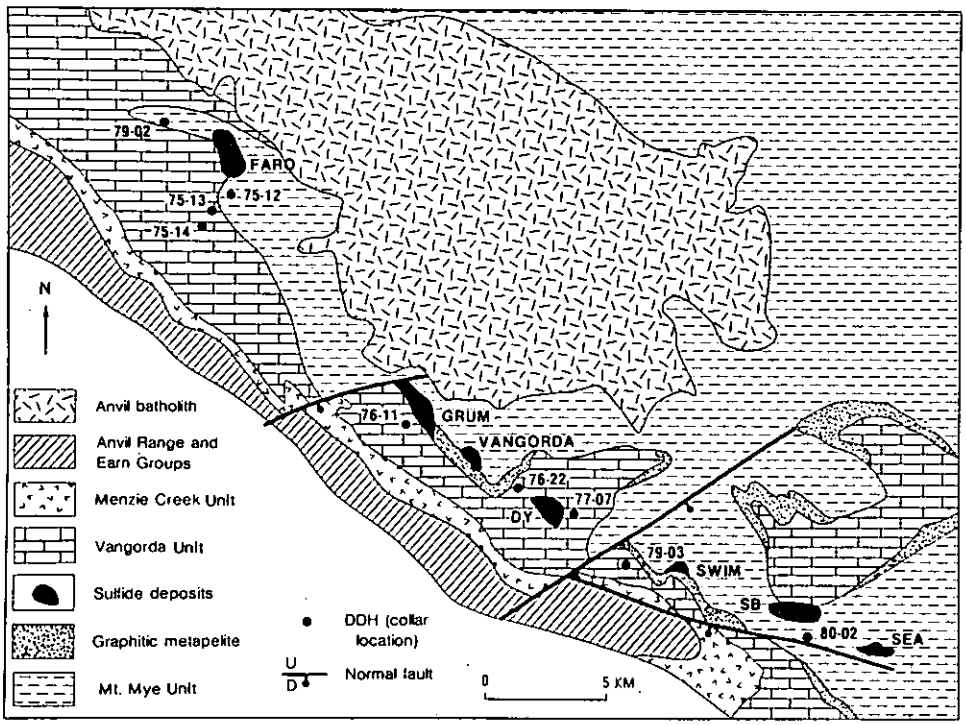

FIG. 2. Geologic map of the Anvil Pb-Zn-Ag district showing surface projections of sulfide mineral deposits and collar locations of drill holes which intersected unmineralized strata. The Anvil batholith is a Middle Cretaceous quartz monzonitic intrusion which thermally and structurally affected the Faro deposit, and to a lesser extent, the Grum deposit.

column, cyclically interspersed with partial ventilation events, then sulfur isotope studies emerge as an extremely important exploration tool in the basin.

Stratigraphy

The Anvil district lies on the southwestern margin of an important lead-zinc-silver province (Carne and Cathro, 1982) known informally as the Selwyn basin (Fig. 1). The district is underlain by late Proterozoic and Paleozoic metasedimentary and lesser metavolcanic rocks (Fig. 2) that formed near the ancient continental margin of North America. The southwestern boundary of the district is defined by the Vangorda Creek fault, part of a major early Mesozoic structure juxtaposing the radically different Yukon-Tanana suspect terrane (Tempelman-Kluit, 1979) with rocks of the district.

The district is underlain by strata as young as Permian, but only those of Ordovician and older age are summarized here (Fig. 3). The older rocks are divided into three mappable units for which informal stratigraphic names are given. The names follow the usage of Jennings and Jilson (1986), who describe the units in some detail. From oldest to youngest these are: the Mt. Mye unit dominated by noncalcareous metapelites, the Vangorda unit dominantly consisting of calcareous metapelites, and the Menzie Creek unit composed of basaltic metavolcanic rocks and graphitic metapelite (Fig. 3). Massive sulfide deposits occur in the Mt. Mye and Vangorda units near the stratigraphic transition zone between the two.

The Mt. Mye unit varies from biotite-muscovite schist to weakly carbonaceous, light to medium gray muscovite-chlorite phyllite with lesser interlayered black graphitic phyllite, marble, calc-silicate phyllite or schist, metabasite, and psammitic schist. Present-day thickness measured perpendicular to S_2 is at least 2 km, and the base of the unit is not exposed in the district.

The upper portion of the unit is very similar to the buff-weathering mudstone and blue-gray mudstone described by Gordey (1978) to the east near Howards Pass, and to unit 8A of Blusson (1966) near Cantung. Tenuous correlation with these units would imply that the top of the Mt. Mye unit is of Early Cambrian or possibly Middle Cambrian age. Parts of the Mt. Mye unit also resemble rocks underlying unit 8A (Blusson, 1966), which suggests that it probably includes rocks as old as Hadrynian.

The Vangorda unit is characterized by light- to medium-gray calcareous pelitic rocks. The most abundant lithology is noncalcareous, weakly carbonaceous, muscovite-chlorite phyllite very thinly interlayered with quartz ± calcite ± dolomite metasiltstone. Major

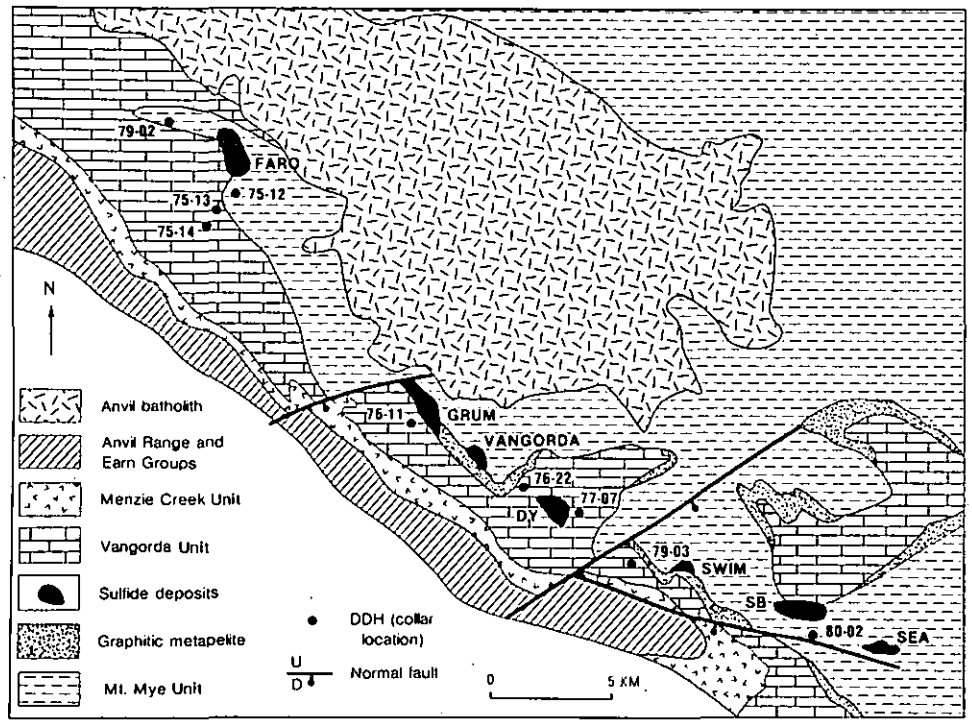

FIG. 2. Geologic map of the Anvil Pb-Zn-Ag district showing surface projections of sulfide mineral deposits and collar locations of drill holes which intersected unmineralized strata. The Anvil batholith is a Middle Cretaceous quartz monzonitic intrusion which thermally and structurally affected the Faro deposit, and to a lesser extent, the Grum deposit.

column, cyclically interspersed with partial ventilation events, then sulfur isotope studies emerge as an extremely important exploration tool in the basin.

Stratigraphy

The Anvil district lies on the southwestern margin of an important lead-zinc-silver province (Carne and Cathro, 1982) known informally as the Selwyn basin (Fig. 1). The district is underlain by late Proterozoic and Paleozoic metasedimentary and lesser metavolcanic rocks (Fig. 2) that formed near the ancient continental margin of North America. The southwestern boundary of the district is defined by the Vangorda Creek fault, part of a major early Mesozoic structure juxtaposing the radically different Yukon-Tanana suspect terrane (Tempelman-Kluit, 1979) with rocks of the district.

The district is underlain by strata as young as Permian, but only those of Ordovician and older age are summarized here (Fig. 3). The older rocks are divided into three mappable units for which informal stratigraphic names are given. The names follow the usage of Jennings and Jilson (1986), who describe the units in some detail. From oldest to youngest these are: the Mt. Mye unit dominated by noncalcareous metapelites, the Vangorda unit dominantly consisting of calcareous metapelites, and the Menzie Creek unit composed of basaltic metavolcanic rocks and graphitic metapelite (Fig. 3). Massive sulfide deposits occur in the Mt. Mye and Vangorda units near the stratigraphic transition zone between the two.

The Mt. Mye unit varies from biotite-muscovite schist to weakly carbonaceous, light to medium gray muscovite-chlorite phyllite with lesser interlayered black graphitic phyllite, marble, calc-silicate phyllite or schist, metabasite, and psammitic schist. Present-day thickness measured perpendicular to S_2 is at least 2 km, and the base of the unit is not exposed in the district.

The upper portion of the unit is very similar to the buff-weathering mudstone and blue-gray mudstone described by Gordey (1978) to the east near Howards Pass, and to unit 8A of Blusson (1966) near Cantung. Tenuous correlation with these units would imply that the top of the Mt. Mye unit is of Early Cambrian or possibly Middle Cambrian age. Parts of the Mt. Mye unit also resemble rocks underlying unit 8A (Blusson, 1966), which suggests that it probably includes rocks as old as Hadrynian.

The Vangorda unit is characterized by light- to medium-gray calcareous pelitic rocks. The most abundant lithology is noncalcareous, weakly carbonaceous, muscovite-chlorite phyllite very thinly interlayered with quartz ± calcite ± dolomite metasiltstone. Major

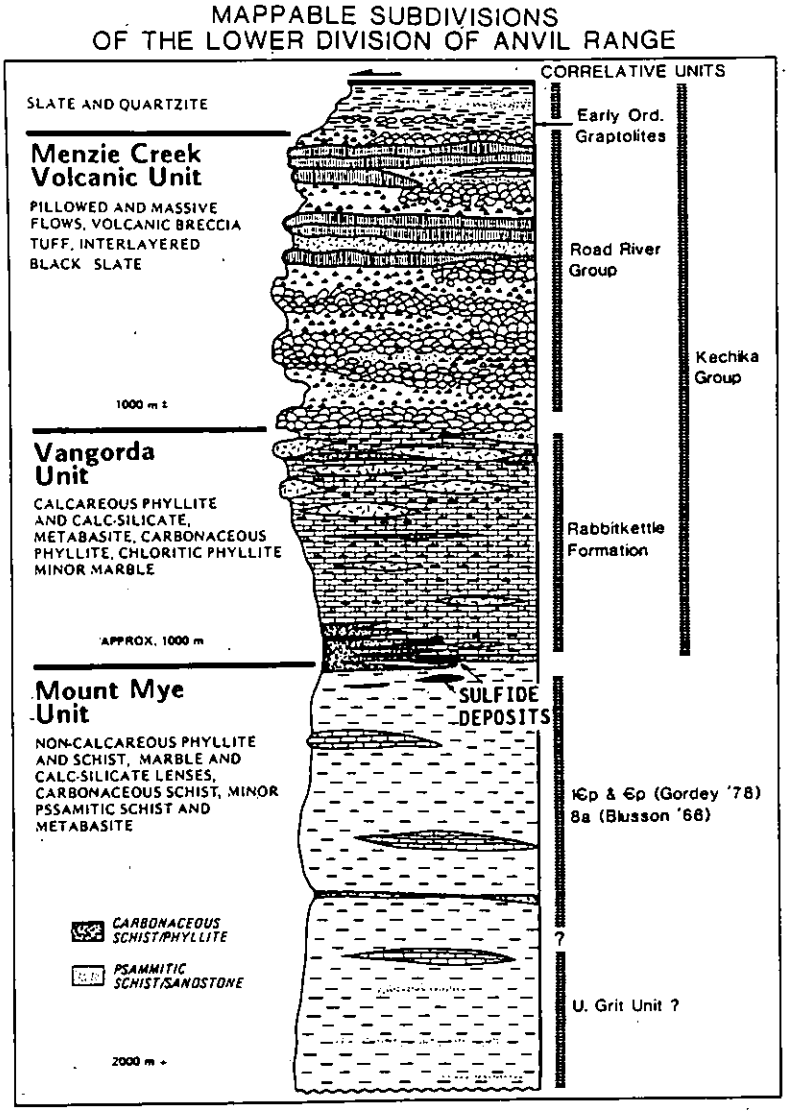

FIG. 3. Informal stratigraphy of the Anvil Pb-Zn-Ag district. Ages range from Late Hadrynian to Early Ordovician, with massive sulfide deposits occurring near the Mount Mye-Vangorda unit transition.

interbanded units include metabasite and metatuff, graphitic phyllite, and phyllitic limestone.

Most metabasite bodies in the Vangorda unit are medium grained and equigranular; thus, they may have been sills. Locally, amygdaloidal margins and a common association with thin-bedded, tuffaceous rocks suggests at least some were flows. Whole-rock compositional data show that the metabasites are all of basaltic composition (Jennings and Jilson, 1986). The bodies range from 1 to 100 m in thickness and are up to several kilometers in length.

The Vangorda unit varies between 0.5 and 2 km in apparent thickness with basic igneous rocks comprising approximately 15 percent of the section. The unit becomes more calcareous up-section, with concomittant increase in metabasaltic units. The Vangorda unit is lithologically similar to, though more argillaceous than, the Middle Cambrian through Early Ordovician Rabbitkettle Formation to the east (Gordey, 1978; Gabrielse et al., 1973).

The Menzie Creek unit is a unit of basaltic metavolcanic rocks consisting of pillowed and massive flows with comparable amounts of massive, coarse, monolithic breccias and lesser, thin-bedded fine tuff and volcanic sandstone and siltstone. Carbonaceous phyllite and brown siltstone which occur about 5 miles northeast of the Anvil batholith contain graptolites of Middle Ordovician or Early Silurian age (Tempelman-Kluit, 1972). These rocks, which are interlayered with the Mt. Mye unit, correlate with the black shale and

chert of the widespread Road River Formation to the northeast (usage of Road River Formation after Gabrielse et al., 1973; see also discussion in Cecile, 1982).

Whole-rock major element and trace element data (Jennings and Jilson, 1986) show that the Menzie Creek unit is composed dominantly of alkali basalt erupted in a within-plate setting similar to the metabasites of the Vangorda unit. The Menzie Creek unit varies from zero to about 1.5 km in thickness in and near the district. It has been traced for 100 km along strike and 30 km across strike, showing that it is one of the largest of several basaltic units of its age in the Yukon. Similar and probably correlative units have been mapped by Cecile (1982) as the Marmot Formation to the northeast and as an unnamed unit to the northwest near Dawson City (Tempelman-Kluit, 1970a).

Deformation, Metamorphism, and Plutonism

The Anvil district has suffered a complex history of intense deformation, metamorphism, and granitic intrusion which must be considered in interpretation of the geochemical data.

Rocks of the district show the effects of at least five periods of deformation. The first two periods are the most pronounced and were accompanied by metamorphism ranging from lower greenschist facies to middle amphibolite facies in a low-pressure, Abukuma-type series.

As has been shown previously (Tempelman-Kluit, 1970b), metamorphic grade increases from the Swim deposit (lower greenschist) to the Faro deposit (amphibolite) with a parallel increase in grain size of the sulfides. As a result, sulfides, sulfates, and host silicates in all deposits are extensively recrystallized and the textures observed are largely metamorphic.

The first deformation (D_1) produced a regional metamorphic foliation (S_1) axial planar to tight to isoclinal mesoscopic folds (F_1) in bedding (S_0) which are rarely preserved in the district. Northeasterly inclined to upright megascopic folds with shallow northwesterly or southeasterly plunging axes appear to have formed at this time.

During the second event (D_2), S_1 was folded to form ubiquitous close to tight mesoscopic folds with shallowly dipping axial planes and subhorizontal axes. A typical cross section of these structures is shown in Figure 4b. The largest megascopic folds known to have formed during D_2 are those at the Grum deposit (Fig. 5) and in the Swim deposit. Parallel to the axial planes of the D_2 folds is a crenulation cleavage (S_2) which imparts a well-developed lithon structure to most rocks of the district, especially the strongly banded phyllites of the Vangorda unit.

The later events (D_3 through D_5) generally produced open folds and weak crenulations in S_2 related to broad, regional structures. Locally, however, the effects may be intense, as in the vicinity of the Faro deposit where the fourth event (D_4) produced tight mesoscopic folds in pervasive S_2 with appreciable growth of mica along S_4 (see Fig. 4a for an example of F_4 folds affecting the outline of the Faro orebody). The third event (D_3) appears related to the formation of the Anvil arch (Tempelman-Kluit, 1972)—a large, doubly plunging antiform which warps S_2 and is cored by the Anvil batholith.

The Anvil batholith ranges in composition from granodiorite to quartz monzonite and textures include equigranular massive, megacrystic massive, and various strongly to weakly foliated variants. The batholith is syn- to late tectonic with respect to D_2. Several K/Ar ages on the granitic rocks yield ages of 85 to 100 m.y. (Tempelman-Kluit, 1972). More recent work indicates Rb-Sr isochron ages of 99 to 100 m.y. for two intrusive phases of the Anvil and nearby Orchay batholiths, with one distinctive sample giving an age of 61 m.y. (Pigage and Anderson, 1985). Massive sulfide deposits occur in a curvilinear trend southwest and south of the Anvil batholith. Some, especially Faro and Grum, were structurally and thermally affected by batholith emplacement.

Massive Sulfide Deposits

The deposits of the Anvil Range lie along the southern flank of the Anvil arch (Fig. 2). From northwest to southeast, they include the Faro, Grum, Vangorda, DY, and Swim deposits. Two other significant sulfide occurrences, the SB and Sea, are known in the district. Tonnage and grade (1981 figures) for each of the deposits are summarized in Table 1 and representative sections through Faro, DY, and Grum are given in Figures 4a, 4b, and 5, respectively.

All deposits are stratiform, strata-bound massive to disseminated sulfide lenses with postdeformational lengths generally two to three times widths. Sulfides are mainly pyrite, sphalerite, and galena; quartz and barite are the principal gangue minerals. Deposits occur as single lenses with little or no interbanded metasedimentary rocks (e.g., Faro, Fig. 4a) or as multilayered lenses with substantial metasedimentary or metavolcanic interlayers (e.g., DY, Fig. 4b; and Grum, Fig. 5). The upper and lower contacts of any given sulfide body are invariably sharp whereas lateral margins appear to grade into the enclosing host rocks. All deposits show variably developed white mica alteration in the immediately adjacent wall rocks. This alteration has not been studied in mineralogical detail but consists of unusually light-colored phyllite or schist enriched in muscovite at the expense of chlorite and biotite. It is not a depositional unit and may have formed either as a reaction product between sedimentary host rocks and deposit-forming hydrothermal fluids, as a metamorphic reaction envelope, or as a

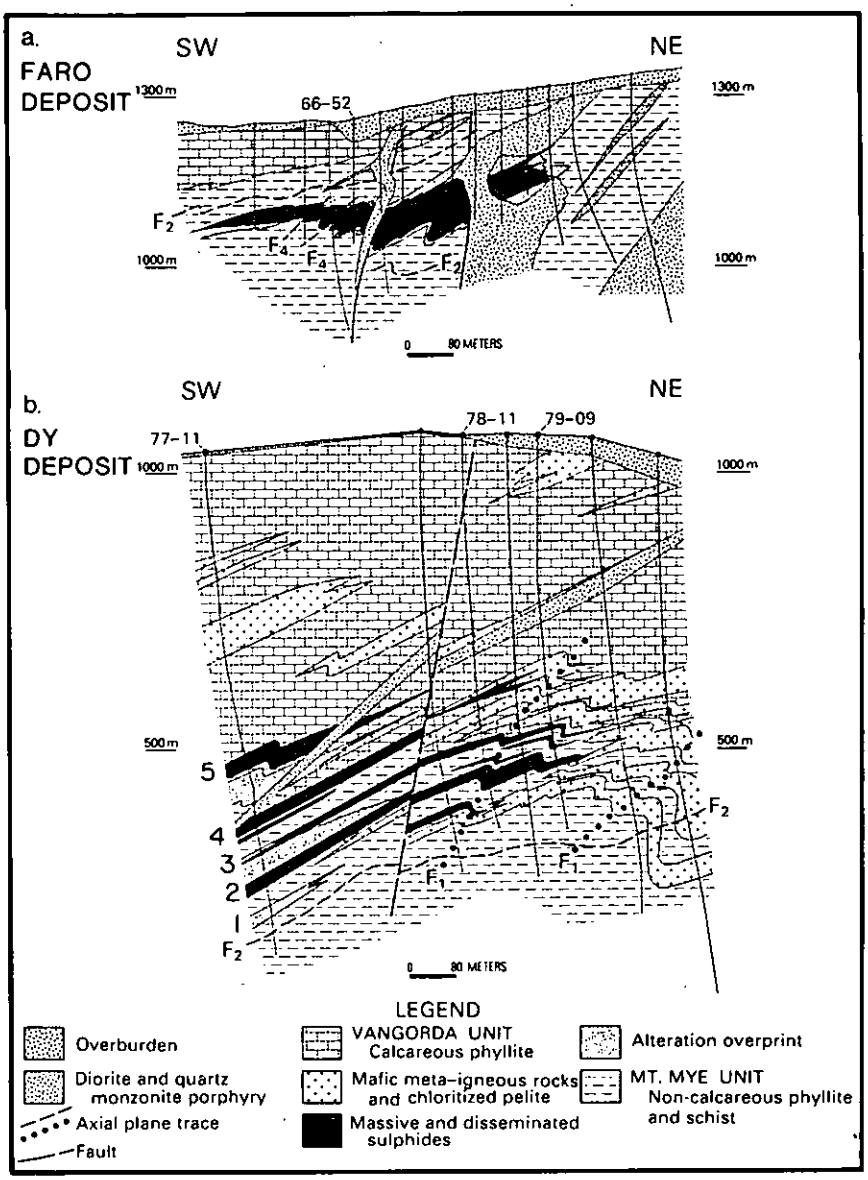

FIG. 4. Generalized cross sections of the Faro and DY deposits, showing the multilayered nature of the DY deposit (five sulfide horizons are arbitrarily numbered from oldest to youngest) in contrast to the single mineralized horizon developed at Faro. Note the close association of mafic meta-igneous rocks with mineralized horizons at DY. F_4 structures are pervasively developed at Faro due to proximity with the Middle Cretaceous Anvil batholith. Drill holes utilized in the present study are numbered.

combination of these processes. In the multilayered deposits, the alteration seems best developed in the footwall of a given lens or deposit, suggesting that hydrothermal alteration is of greater importance.

The Anvil deposits occur through a stratigraphic interval of about 150 m straddling the contact between the Mt. Mye and Vangorda units. Thin graphitic phyllite is regionally developed at that horizon, but near the deposits graphitic layers are much thicker and more numerous. Sulfide lenses tend to be developed as lateral equivalents to or immediately adjacent to graphitic units (Figs. 2–6).

Most basaltic meta-igneous rocks occur stratigraphically above the Anvil deposits. The first significant pulse of extrusive basaltic activity produced thin metabasites in the uppermost Mt. Mye unit, suggesting at least a temporal relationship between ore formation and basaltic magmatism (Jennings et al., 1980). It should be emphasized, however, that there is generally a poor spatial association of sulfide deposits and

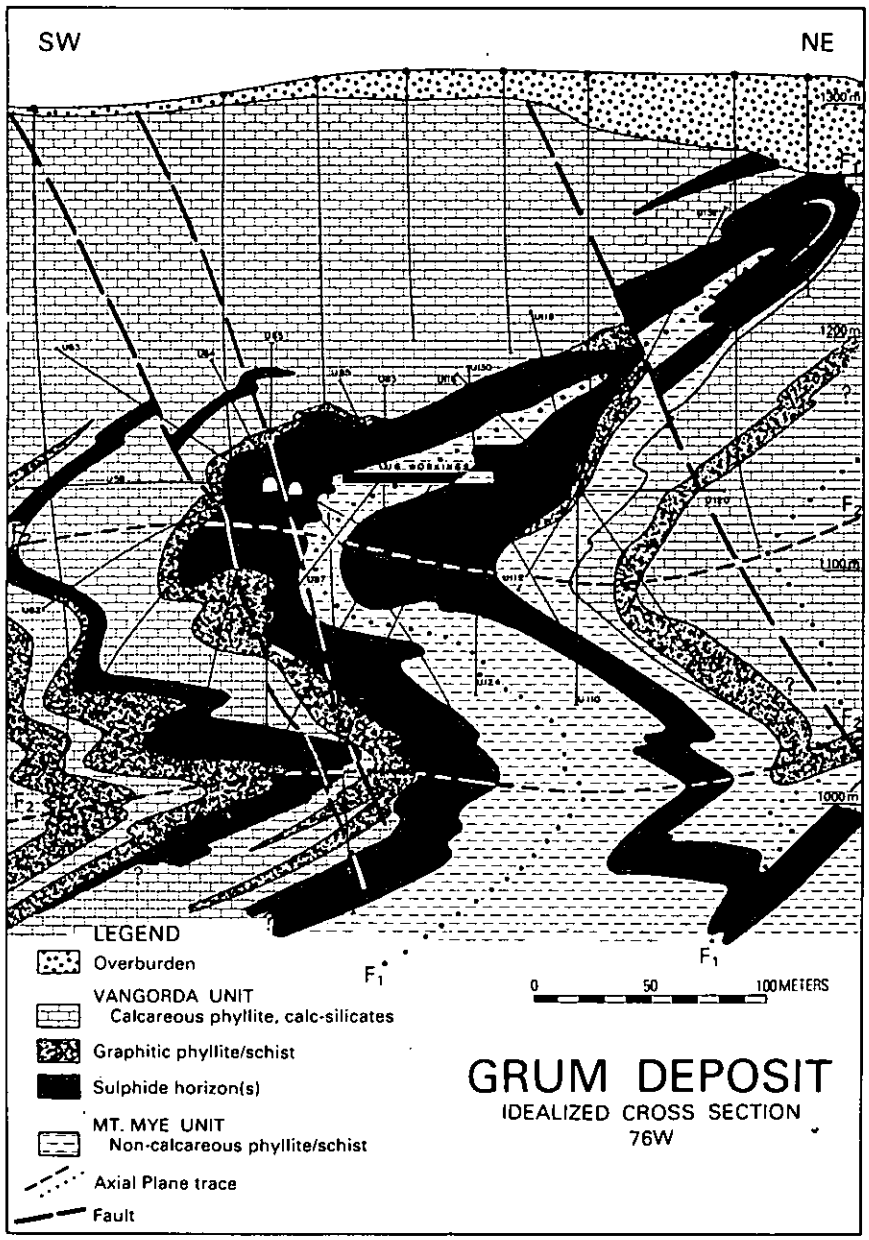

FIG. 5. Generalized cross section of the Grum deposit. The Grum deposit is folded about steeply southwesterly dipping S_1 axial planes with northwesterly plunging F_1 fold axes. The F_1 folds have been cut and crenulated by a shallow southwesterly dipping S_2 crenulation foliation producing F_2 folds nearly coaxial with F_1. Three distinct sulfide horizons are apparent: upper—southwesterly lens hosted entirely in the Vangorda unit, Central—Vangorda in the hanging wall and Mount Mye in the footwall, and lower—northeasterly lens hosted entirely in the Mount Mye unit. The Grum horizons show preferential development of the distal ribbon-banded facies relative to Faro (Table 4). Both surface and underground drill holes were utilized in this study.

metabasaltic rocks. The DY deposit, with sulfide lenses in direct contact with chloritic phyllite lenses (Fig. 4b), is the notable exception to this generalization. Nonetheless, the Anvil deposits all are dominantly sediment hosted.

In map view, the deposits form a curvilinear array along the Mt. Mye-Vangorda boundary (Fig. 2). Detailed mapping and drilling suggest that the deposits lie close to a "pinch out" or "zero edge" of the associated graphitic phyllite. To date, no sulfide litho-

facies have been encountered in drill holes through the transition zone southwest of the deposit line. Taken together, these observations suggest some relationship between sulfide deposits, facies changes at reduced basin margins, and basaltic volcanism.

While deposits of the Anvil belt show distinct differences in terms of the numbers of mineralized horizons per deposit, spatial relations to metabasaltic rocks, and grades of regional metamorphism, the overall similarity of sulfide lithofacies is striking. All lithofacies are commonly banded and show narrowly gradational, vertical contacts. The principal facies include: (1) ribbon-banded, sulfide-bearing graphitic quartzite: alternating laminae on a millimeter to centimeter scale of dark gray to black, siliceous, carbonaceous pelite to argillaceous metachert and light gray, pyrite-, sphalerite-, and galena-bearing quartzite; (2) muscovite, pyritic quartzite: disseminated (5%) to nearly massive (60%) pyrite and highly variable sphalerite and galena in a light gray, muscovite quartzite matrix; (3) massive pyritic sulfide: massive pyritic sulfide (>80% total sulfide by volume) generally enriched in sphalerite and galena relative to the previous unit with quartz as gangue, unit may grade into massive nonpyritic base metal sulfide or massive pyrrhotite; and (4) baritic and ferroan carbonate-bearing massive pyritic sulfide: massive sulfide, sulfate, and carbonate commonly enriched in sphalerite and galena with subsidiary magnetite and quartz gangue.

Arrangement of sulfide lithofacies in a vertical and lateral sense commonly occurs within all of the deposits and is referred to as the "Anvil cycle." Details of the Anvil cycle are best seen in an idealized model of an Anvil deposit (Fig. 6) based heavily on the Faro deposit. The base of a cycle is marked by ribbon-banded, sulfide-bearing graphitic quartzite succeeded upward by pyritic quartzite, massive pyritic sulfide, and baritic massive sulfide. This vertical array is also seen laterally with ribbon-banded, sulfide-bearing graphitic quartzite forming the marginal or distal facies of a deposit, with inward transition to baritic massive sulfide. The similarity of Anvil cycle development between deposits strongly suggests a consanguinous origin for the Anvil district deposits.

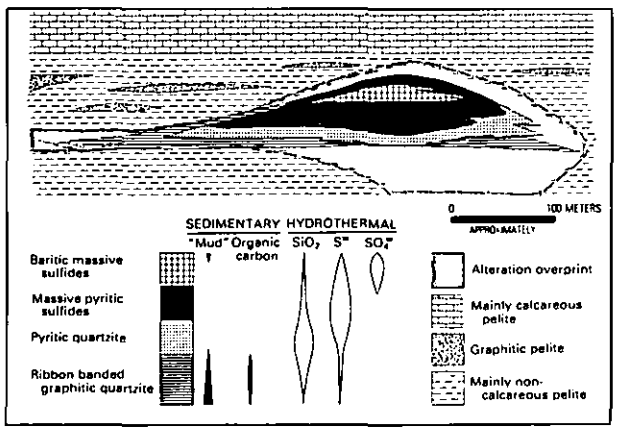

FIG. 6. The Anvil cycle: an idealized model of the distribution of sulfide lithofacies in Anvil district sulfide deposits.

Poorly developed metal zoning follows the facies distribution pattern in that the base of a cycle tends to be high in zinc with lead and silver enrichment developed toward the top. Copper and gold seem to be preferentially enriched in the siliceous facies of the footwall alteration zone or in the pyritic quartzite facies of the stratiform sulfides (Jennings and Jilson, 1986).

The Anvil cycle facies zonation pattern, although common and well defined, is somewhat idealized. It is important to note that Anvil cycles are developed on a variety of scales and to varying degrees of completeness. A series of complete and partial cycles may cumulatively form a megacycle either on the scale of a deposit (e.g., Faro) or on the scale of a single sulfide horizon within a multilayered deposit (e.g., DY). Complete cycles also are seen over a 1-m stratigraphic interval (or less), forming cycles within other cycles.

Methods

A broad variety of drill core samples, from both mineralized and unmineralized areas of the Anvil Range, were utilized in this study. In all, 487 sulfur isotope analyses were completed on 305 samples. Samples were selected from the various deposits as follows: Faro, 23; Grum, 71; and DY, 138. The remaining 73 samples are from unmineralized carbonaceous pelites in drill holes in the areas of the Faro, Grum, and DY deposits; drill-hole collar locations for barren holes are shown in Figure 2. Samples from the Faro and Grum deposits were taken directly from drill core and generally represent a few centimeters of stratigraphic interval. Mechanical mineral separations were carried out on the Grum samples, where possible. DY samples were taken from assay pulps which represent homogenized channel samples of larger intervals, usually a meter or two, but always restricted to a single lithologic unit.

Because many of the samples were finely ground assay pulps, it was necessary to separate sulfur-bearing phases for isotopic analysis by chemical extraction. Samples were reacted first with hot 6 *N* HCl while purging with pure N_2 gas. The N_2 gas was passed downstream through an $AgNO_3$ trap to precipitate the sulfide released from galena and sphalerite. Pyrrhotite, present in a few samples, also reacts in this step. Bulk sulfide and pyrite residues from hot HCl leaches were oxidized with boiling aqua regia-bro-

TABLE 2. Geochemical and Lithological Data for Unmineralized Anvil Range Samples[1]

Core no.	Depth (m)	% $C_{organic}$	% C in CO_3	% S_{total}	S/C_{atomic}	$\delta^{34}S^2$ (‰)	Lithology
79-02	164.4–165.9		0.19	0.30		34.1	Mt. Mye unit: noncalcareous muscovite + chlorite ± biotite phyllite
79-02	165.9–167.2	0.08	0.59	0.30	1.40	14.6	Mt. Mye unit: noncalcareous muscovite + chlorite ± biotite phyllite
79-02	167.2–168.5	0.06	2.29	0.20	1.25	13.5	Mt. Mye unit: noncalcareous muscovite + chlorite ± biotite phyllite
79-02	168.5–170.0	0.04	0.76	0.20	1.87	12.7	Mt. Mye unit: noncalcareous muscovite + chlorite ± biotite phyllite
79-02	227.9–229.3	0.11	0.04	0.30	1.02	18.7	Mt. Mye unit: carbonaceous, biotite-muscovite-andalusite schist
79-02	229.3–230.9		0.11	0.30		13.9	Mt. Mye unit: carbonaceous, biotite-muscovite-andalusite schist
79-02	230.9–232.3	0.02	0.18	0.10	1.87	22.4	Mt. Mye unit: carbonaceous, biotite-muscovite-andalusite schist
79-02	232.3–233.7		0.11	0.30			Mt. Mye unit: carbonaceous, biotite-muscovite-andalusite schist
79-02	303.1–304.6		0.67	0.50		12.5	Mt. Mye unit: carbonaceous, biotite-muscovite-andalusite schist
79-02	304.6–306.0	0.83	0.23	0.20	0.09	11.4	Mt. Mye unit: carbonaceous, biotite-muscovite-andalusite schist
79-02	306.0–307.4	1.16	0.12	0.60	0.19	13.2	Mt. Mye unit: carbonaceous, biotite-muscovite-andalusite schist
79-02	307.4–308.9		0.26	0.60			Mt. Mye unit: carbonaceous, biotite-muscovite-andalusite schist
79-02	364.5–365.9	0.71	0.20	1.70	0.90	7.4	Mt. Mye unit: graphitic schist
79-02	365.9–367.4	1.34	0.24	1.40	0.39	4.2	Mt. Mye unit: graphitic schist
79-02	367.4–369.4	1.53	0.28	1.20	0.29	11.7	Mt. Mye unit: graphitic schist
75-12	69.5–70.3		0.45	0.30		13.4	Mt. Mye unit: carbonaceous, biotite-muscovite-andalusite schist
75-12	70.3–71.3	0.08	0.52	0.30	1.40	12.9	Mt. Mye unit: carbonaceous, biotite-muscovite-andalusite schist
75-12	78.3–79.2	0.16	1.51	0.20	0.47	15.7	Mt. Mye unit: carbonaceous, biotite-muscovite-andalusite schist

TABLE 2—(*Cont.*)

Core no.	Depth (m)	% $C_{organic}$	% C in CO_3	% S_{total}	S/C_{atomic}	$\delta^{34}S^2$ (‰)	Lithology
75-12	79.2–80.2			1.30		13.2	Mt. Mye unit: carbonaceous, biotite-muscovite-andalusite schist
75-12	87.2–88.1	0.05	1.79	0.70	5.24	16.6	Mt. Mye unit: carbonaceous, biotite-muscovite-andalusite schist
75-12	88.1–89.0	0.08	0.43	0.40	1.87	15.4	Mt. Mye unit: carbonaceous, biotite-muscovite-andalusite schist
75-12	110.7–111.6		1.68	0.30		18.7	Mt. Mye unit: very carbonaceous, biotite-muscovite-andalusite schist
75-12	111.6–112.5	0.40	0.40	0.10	0.09	18.2	Mt. Mye unit: very carbonaceous, biotite-muscovite-andalisite schist
75-13	93.0–93.9			0.80		15.2	Mt. Mye unit: graphitic schist
75-13	105.1–106.0	0.04	0.57	0.10	0.94	10.9	Mt. Mye unit: carbonaceous, biotite-muscovite-andalusite schist
75-13	106.0–107.0		0.40	0.50		13.7	Mt. Mye unit: carbonaceous, biotite-muscovite-andalusite schist
75-13	115.3–116.3		0.74	0.50		15.4	Mt. Mye unit: carbonaceous, biotite-muscovite-andalusite schist
75-13	116.3–117.2		0.99	0.20		11.8	Mt. Mye unit: carbonaceous, biotite-muscovite-andalusite schist
75-13	125.1–125.9	0.43	0.83	1.80	1.57	17.1	Mt. Mye unit: graphitic schist
75-13	125.9–126.5	0.20	1.94	0.40	0.75	15.7	Mt. Mye unit: graphitic schist
75-14	83.5–84.1	0.08	0.32	0.30	1.40	13.4	Mt. Mye unit: carbonaceous, biotite-muscovite-andalusite schist
75-14	84.1–84.6		0.84	0.10		12.3	Mt. Mye unit: carbonaceous, biotite-muscovite-andalusite schist
75-14	102.6–103.2		0.11	0.30		17.8	Mt. Mye unit: carbonaceous, biotite-muscovite-andalusite schist
75-14	119.1–119.7	0.46	0.38	0.20	0.16	31.4	Mt. Mye unit: carbonaceous, biotite-muscovite-andalusite schist
75-14	120.4–120.9		2.21	0.10			Mt. Mye unit: carbonaceous, biotite-muscovite-andalusite schist to graphite schist

TABLE 2—(*Cont.*)

Core no.	Depth (m)	% $C_{organic}$	% C in CO_3	% S_{total}	S/C_{atomic}	$\delta^{34}S^2$ (‰)	Lithology
75-14	138.2–139.5	0.41	1.19	2.40	2.19	7.7	Mt. Mye unit: carbonaceous, biotite-muscovite-andalusite schist to graphite schist
76-11	325.1–326.7	1.92	2.14	1.30	0.25	15.8	Vangorda unit: carbonaceous to graphitic argillite-phyllite
76-11	326.7–328.2	1.98	1.93	1.90	0.36	17.0	Vangorda unit: carbonaceous to graphitic argillite-phyllite
76-11	355.3–356.8	1.22	1.08	2.40	0.74	13.8	Vangorda unit: carbonaceous to graphitic argillite-phyllite
76-11	356.8–358.4	2.32	1.30	1.10	0.18	12.4	Vangorda unit: carbonaceous to graphitic argillite-phyllite
76-22	78.2–79.6		0.10	0.40		24.0	Vangorda unit: calcareous muscovite + chlorite ± biotite phyllite
76-22	79.6–81.1	0.01	1.00	0.20	7.49	23.5	Vangorda unit: calcareous muscovite + chlorite ± biotite phyllite
76-22	81.1–82.5		0.97	0.10		16.9	Vangorda unit: calcareous muscovite + chlorite ± biotite phyllite
76-22	175.4–178.4	1.29	0.87	0.40	0.12	15.5	Vangorda unit: carbonaceous to graphitic argillite-phyllite
76-22	273.2–275.9		0.21	0.50		13.2	Vangorda unit: calc-silicate phyllite-schist (chloritic)
76-22	275.9–278.8	0.58		0.60	0.39	11.1	Vangorda unit: calc-silicate phyllite-schist (chloritic)
77-07	198.9–200.4	0.18	2.23	0.50	1.04	27.7	Vangorda unit: calcareous muscovite + chlorite ± biotite phyllite
77-07	200.4–202.0	0.01	3.22	0.10	3.74	27.2	Vangorda unit: calcareous muscovite + chlorite ± biotite phyllite
77-07	202.0–203.4	0.03	2.74	0.10	1.25	27.3	Vangorda unit: calcareous muscovite + chlorite ± biotite phyllite
77-07	203.4–204.8			0.10			Vangorda unit: calcareous muscovite + chlorite ± biotite phyllite
77-07	354.6–357.2	0.53	3.22	0.60	0.42	11.6	Vangorda unit: carbonaceous to graphitic argillite-phyllite
77-07	389.3–391.3	1.31	1.17	0.30	0.09	19.9	Vangorda unit: carbonaceous to graphitic argillite-phyllite
77-07	459.7–461.2		2.25	0.40		16.9	Vangorda unit: calc-silicate phyllite-schist (siliceous, muscovite alteration)
77-07	461.2–462.6	0.05	1.16	0.10	0.75	16.5	Vangorda unit: calc-silicate phyllite-schist (siliceous, muscovite alteration)
77-07	462.6–463.2	0.02	0.36	0.20	3.74	15.8	Vangorda unit: calc-silicate phyllite-schist (siliceous, muscovite alteration)
80-12	358.8–360.8	0.08	1.21	0.20	0.94	22.0	Vangorda unit: calcareous muscovite + chlorite ± biotite phyllite

TABLE 2—(*Cont.*)

Core no.	Depth (m)	% $C_{organic}$	% C in CO_3	% S_{total}	S/C_{atomic}	$\delta^{34}S^2$ (‰)	Lithology
80-12	360.8–361.8	0.08	2.29	0.40	1.87	26.9	Vangorda unit: calcareous muscovite + chlorite ± biotite phyllite
80-12	361.8–363.3		2.02	0.20		24.2	Vangorda unit: calcareous muscovite + chlorite ± biotite phyllite
80-12	363.3–364.7	0.01	1.13	0.10	3.74	25.9	Vangorda unit: calcareous muscovite + chlorite ± biotite phyllite
80-12	767.5–769.0	2.76	0.35	0.70	0.09	−0.8	Vangorda unit: carbonaceous to graphitic argillite-phyllite (sulfidic, siliceous)
80-12	769.0–770.5	0.87	2.59	2.60	1.12	16.2	Vangorda unit: carbonaceous to graphitic argillite-phyllite (sulfidic, siliceous)
80-12	770.5–771.5	1.75	0.42	2.20	0.47	16.7	Vangorda unit: carbonaceous to graphitic argillite-phyllite (sulfidic, siliceous)
80-12	819.6–821.1	1.68	5.48	1.00	0.22	13.3	Vangorda unit: carbonaceous to graphitic argillite-phyllite (siliceous)
80-12	821.2–822.6	0.76	0.86	1.00	0.49	11.5	Vangorda unit: carbonaceous to graphitic argillite-phyllite (siliceous)
80-12	822.6–823.6	0.63	0.68	1.90	1.13	9.4	Vangorda unit: carbonaceous to graphitic argillite-phyllite (siliceous)
80-12	978.6–980.0	0.01	0.25	0.70	26.20	14.4	Mt. Mye unit: noncalcareous muscovite + chlorite ± biotite phyllite-schist
80-12	980.0–981.5	0.05	0.09	0.40	2.99	14.5	Mt. Mye unit: noncalcareous muscovite + chlorite ± biotite phyllite-schist
80-12	981.5–982.6		0.30	0.10		15.5	Mt. Mye unit: noncalcareous muscovite + chlorite ± biotite phyllite-schist
80-12	982.6–983.9	0.01	0.16	0.20	7.49	16.2	Mt. Mye unit: noncalcareous muscovite + chlorite ± biotite phyllite-schist
79-03	112.0–114.8	2.65	4.08	2.00	0.28	19.6	Vangorda unit: carbonaceous to graphitic argillite-phyllite
80-02	236.8–238.0	1.67	0.37	1.30	0.29	8.6	Vangorda unit: carbonaceous to graphitic argillite-phyllite (sulfidic)
80-02	238.0–239.6	0.19	3.94	0.90	1.77	10.1	Vangorda unit: carbonaceous to graphitic argillite-phyllite (sulfidic)

[1] Refer to Figure 2 for core locations
[2] Pyrite extracted as total sulfide in aqua regia

mine solution and the resulting sulfate precipitated as barium sulfate. Barium sulfate and natural barites, leached of sulfides by boiling aqua regia-bromine solution, were reduced with graphite under pure N_2 gas at 1,100°C. The sulfide was precipitated as Ag_2S. In all cases the amounts of sulfide derived from the galena-sphalerite fraction and from the pyrite fraction were quantified. This allowed calculation of the total sulfide sulfur content and the bulk sulfur isotope value of sulfide minerals. In other cases the bulk sulfide sulfur content and sulfur isotope values were measured directly by reaction of bulk samples with aqua regia (Tables 2–5).

Silver sulfides were combusted in vacuo with cuprous oxide at 850° to 1,050°C to produce SO_2, which was purified by conventional vacuum distilla-

TABLE 3. Geochemical and Lithologic Data for Drill Hole 66-52 from the Faro Deposit[1]

Core no.	Depth (m)	% S in pyrite	% S_{total}	$\delta^{34}S$ (‰) SlGnPo[2]	Pyrite	Total S	Barite	Lithology
66-52	165.8	35.52	42.01	14.3	16.6	16.2	24.5	Baritic massive sulfides
66-52	165.9	38.52	41.96	14.7	17.1	16.9	23.5	Baritic massive sulfides
66-52	166.8	42.47	50.29	18.5	19.7	19.5		Massive sulfide, porphyroblastic
66-52	167.8	42.11	50.78	19.2	16.4	16.9		Massive sulfide, porphyroblastic
66-52	169.3	48.78	53.30	13.4	14.9	14.7		Massive sulfide, porphyroblastic
66-52	170.8	44.31	52.65	16.5	17.9	17.7		Massive sulfide, porphyroblastic
66-52	172.3	39.38	44.91	18.4	19.7	19.5		Massive sulfide, porphyroblastic
66-52	173.2	31.67	36.95	16.6	18.5	18.2	26.2	Baritic massive sulfides
66-52	174.2	50.51	56.21	17.5	18.5	18.4		Massive sulfide, porphyroblastic
66-52	175.1	45.45	49.98	13.5	19.9	19.3		Massive sulfide, porphyroblastic
66-52	176.4	29.07	37.30	18.7	16.3	16.8	25.7	Baritic massive sulfides
66-52	177.2	50.31	57.83	14.8	19.8	19.1		Massive sulfide, porphyroblastic
66-52	178.7	28.60	34.10	14.4	20.0	19.1	24.7	Baritic massive sulfides
66-52	180.3	26.37	29.74	15.0	17.1	16.9	26.8	Baritic massive sulfides
66-52	182.1	48.12	50.07	13.1	14.0	14.0		Massive sulfide, porphyroblastic
66-52	183.6	51.26	57.87	15.2	15.9	15.8		Massive sulfide, porphyroblastic
66-52	185.1	42.81	45.97	12.8	13.7	13.6		Massive sulfide, porphyroblastic
66-52	186.2	9.28	20.02	14.2	14.9	14.5		Pyritic quartzite
66-52	186.7	0.43	1.02	15.0	14.9	15.0		Sulfidic, graphitic, banded quartzite
66-52	187.6	0.16	0.71	15.1	15.1	15.1		Sulfidic, graphitic, banded quartzite
66-52	189.1	1.59	2.57	14.3	15.1	14.8		Pyritic quartzite
66-52	190.0	1.21	2.23	13.7	15.7	14.8		Pyritic quartzite
66-52	190.6	0.60	1.83	14.2	15.7	14.7		Sulfidic, graphitic, banded quartzite
66-52	191.5	4.08	4.08		13.6	13.6		Sulfidic, graphitic, banded quartzite

[1] See Figure 4 for drill hole location
[2] SlGnPo = sphalerite + galena ± pyrrhotite; volatilized in 6 *N*, 60°C HCl

tion. Yields of SO_2, routinely monitored, were generally in the range 95 to 102 percent. Isotope ratio mass spectrometry was done on the MAT 250 instruments in the laboratory of Eugene Perry at Northern Illinois University and in the Biochemistry Department, University of Wisconsin, Madison, and on a Nuclide 6-60-RMS at the Department of Geology and Geophysics, University of Wisconsin, Madison. Isotope values are reported in the conventional delta notation, standardized to Canyon Diablo troilite (CDT) using a regression line determined from the McMaster University sulfur isotope reference series (Rees, 1978). Modern seawater sulfate is calibrated to 21.0 per mil on this scale. Analytical precision is ±0.15 per mil based on replicate analyses.

Carbon content was analyzed in the DY samples and the unmineralized samples. Unmineralized samples were analyzed for total carbon and carbonate carbon, with organic carbon calculated by difference (Table 2). DY samples were analyzed for organic carbon content using the residues from the 6 *N* HCl leach, which removed carbonate minerals (Table 5). Analysis was done on CO_2 evolved by induction heating using a LECO analyzer.

All lead isotope analyses were performed on galena-bearing samples. In most cases, sufficient lead was dissolved from the samples using HCl, but in others, aqua regia was used. In all cases, lead was purified using anion exchange columns and aniodic electrodeposition. Samples were analyzed using single filament silica gel techniques on a 90°, 12-in. mass spectrometer in the Geophysics-Geology Geochronology Laboratory at the University of British Columbia. In-run precision was generally 0.1 percent or better (1σ). Broken Hill No. 1 standard was analyzed 17 times with equivalent precision during and prior to the study. The results are: $^{206}Pb/^{204}Pb = 16.013 \pm 0.010$, $^{207}Pb/^{204}Pb = 15.406 \pm 0.009$, and $^{208}Pb/^{204}Pb = 35.685 \pm 0.058$. Based on these results, the reproducibility of sample analyses is considered to be 0.1 percent or better.

Lead Isotope Results

Thirty-eight galena samples were analyzed from the Anvil area (Table 6). The results for Anvil deposit galena samples are: $^{206}Pb/^{204}Pb = 18.327$ to 18.586, $^{207}Pb/^{204}Pb = 15.591$ to 15.717, and $^{208}Pb/^{204}Pb = 38.136$ to 38.899. These data have been presented previously in construction of lead isotope growth curves for shale-hosted lead-zinc deposits of the Canadian Cordillera (Godwin and Sinclair, 1982), but detailed interpretations of the Anvil data in terms of ore genesis have not been made.

Results are also available from the earlier work of LeCouter (1973), who analyzed nine samples from Faro, five samples from Vangorda, four samples from

TABLE 4. Geochemical and Lithologic Data for the Grum Deposit

Core no.	Depth[1] (m)	Sulfide horizon	$\%S_{total}$[2]	$\delta^{34}S$ (‰) Pyrite[3]	Sphalerite[3]	Galena[3]	Total S	Barite	Lithology
Section 66W									
A99	140.5	Lower	26.63	21.9			20.2		Pyritic massive sulfide (sphalerite-galena bearing)
A99	142.1	Lower	25.28	15.5			15.5	30.6	Baritic massive sulfide (sphalerite-galena bearing)
A99	145.3	Lower	31.24	13.3			13.4		Pyritic massive sulfide (sphalerite-galena bearing)
A99	153.5	Lower	21.70	19.0			16.5	32.0	Baritic massive sulfides (sphalerite-galena bearing)
A99	154.5	Lower	40.36	14.8			15.2		Pyritic massive sulfide (magnetite bearing)
A99	157.1	Lower	27.02	14.8			14.8		Pyritic quartzite
A99	162.1	Lower	15.46	13.8			14.0		Pyritic quartzite (sphalerite-galena bearing)
A99	169.5	Lower	32.84	15.1			15.3		Pyritic quartzite (pyrrhotitic)
A99	178.1	Lower	12.29	16.4			16.3		Muscovite-rich sulfide-bearing quartzite (sphalerite-galena bearing)
A109	136.1	Lower	21.80				18.1	32:1	Baritic massive sulfides (sphalerite-galena bearing)
A109	147.8	Lower	14.22				16.9		Pyritic massive sulfide (sphalerite-galena magnetite bearing)
A109	149.0	Lower	10.56				15.4		Ribbon-banded graphitic, sulfidic quartzite (fine-grained pyrite)
A109	154.3	Lower	5.34				14.9		Muscovite-rich sulfide-bearing quartzite (siliceous)
A109	155.8	Lower	14.55				17.1		Muscovite-rich sulfide-bearing quartzite (siliceous, magnetite bearing)
A135	139.7	Lower	13.01				19.0	31.7	Baritic massive sulfides (sphalerite-galena magnetite bearing)
A135	146.9	Lower	25.50				15.8		Pyritic massive sulfide
A135	148.6	Lower	18.86				12.9		Sphalerite-galena-bearing pyritic quartzite
A135	150.8	Lower	18.19				17.5		Pyritic quartzite
A135	152.5	Lower	10.97				16.5		Ribbon-banded graphitic, sulfidic quartzite (siliceous, fine-grained pyrite)
Section 74W									
U15	29.3	Upper	16.90				14.6		Muscovite-rich sulfide-bearing quartzite (pyrrhotitic, sphalerite-galena bearing)
U15	28.8	Upper	33.43		15.5		19.2		Baritic massive sulfides (sphalerite-galena bearing)
U15	27.9	Upper	28.57	15.9			16.4		Pyritic massive sulfide (sphalerite-galena magnetite bearing)
U15	27.4	Upper	10.29				20.3	35.2	Baritic massive sulfides (sphalerite-galena bearing)
U15	24.7	Upper	29.96		14.3	14.1	15.9		Pyritic massive sulfide (sphalerite-galena magnetite bearing)
U15	9.3	Upper	6.18				12.5		Muscovite-rich sulfide-bearing quartzite (siliceous, pyrrhotitic)
U28	17.4		15.16				15.5		Muscovite-rich sulfide-bearing quartzite (chalcopyrite bearing)

TABLE 4—(*Cont.*)

Core no.	Depth[1] (m)	Sulfide horizon	$\%S_{total}$[2]	$\delta^{34}S$ (‰) Pyrite[3]	Sphalerite[3]	Galena[3]	Total S	Barite	Lithology
U43	22.2	Central	30.74				16.7		Pyritic massive sulfide (sphalerite-galena bearing, baritic)
U43	21.6	Central	16.74				16.1		Ribbon-banded graphitic, sulfidic quartzite
U43	20.2	Central	31.50				14.4		Pyritic massive sulfide (siliceous, sphalerite-galena bearing)
U43	18.6	Central	28.81				16.5		Pyritic massive sulfide (sphalerite-galena bearing)
U43	13.4	Central	23.45				15.8		Pyritic massive sulfide (siliceous, sphalerite-galena bearing)
U43	11.1	Central	14.95				19.0		Ribbon-banded graphitic, sulfidic quartzite (sphalerite-galena bearing)
U43	6.8	Central	14.05				16.0		Pyritic quartzite
Section 80W									
A24	328.9	Central	16.85	11.8	10.8	9.4	10.5		Sphalerite-galena bearing pyritic quartzite
A24	329.5	Central	31.85				16.0	31.2	Baritic massive sulfides (sphalerite-galena bearing)
A24	330.3	Central	27.09				15.8		Pyritic quartzite
A24	331.8	Central	19.34	15.8	14.3	12.4	14.0		Nonpyritic quartzite (sphalerite-galena bearing)
A24	333.1	Central	40.95				15.8		Pyritic massive sulfide (sphalerite-galena bearing)
A24	335.2	Central	44.50	15.3			15.1		Pyritic massive sulfide (sphalerite-galena bearing)
A24	337.1	Central	18.96	16.6	15.6	14.5	15.9		Sphalerite-galena bearing pyritic quartzite
A24	338.6	Central	32.70	16.9	15.3		15.7		Pyritic massive sulfide (sphalerite-galena bearing)
A24	340.8	Central	13.70	14.9	15.4		13.6		Ribbon-banded graphitic, sulfidic quartzite (siliceous, sphalerite-galena bearing)
A24	341.4	Central	32.55		14.0	12.7	14.5		Pyritic massive sulfide (sphalerite-galena bearing)
A24	342.9	Central	16.82	13.5			13.1		Ribbon-banded graphitic, sulfidic quartzite (siliceous, sphalerite-galena bearing)
A24	343.5	Central	30.02		13.8	13.3	14.1		Sphalerite-galena bearing pyritic quartzite
U142	122.7	Central	35.72	19.2			19.2	34.7	Baritic massive sulfides
U142	117.9	Central	44.79	19.6			19.3		Pyritic massive sulfide (sphalerite-galena bearing, baritic)
U142	108.0	Central	30.47	15.5			15.3		Ribbon-banded graphitic, sulfidic quartzite
U142	96.5	Central	11.25	7.3	14.0		14.0		Muscovite-rich sulfide-bearing quartzite (siliceous, porphyroblastic pyrite)
U151	64.2	Upper	48.03				11.6		Carbonate-bearing massive pyritic sulfide
U151	60.6	Upper	31.89				18.3		Pyritic massive sulfide (sphalerite-galena magnetite bearing)
U151	59.0	Upper	49.11				13.2		Pyritic massive sulfide
U141	58.0	Upper	13.79				17.2	32.6	Baritic massive sulfides (sphalerite-galena bearing)
U151	55.2	Upper	18.97				15.6		Baritic massive sulfides (sphalerite-galena bearing)

TABLE 4—(*Cont.*)

Core no.	Depth[1] (m)	Sulfide horizon	$\%S_{total}$[2]	$\delta^{34}S$ (‰) Pyrite[3]	Sphalerite[3]	Galena[3]	Total S	Barite	Lithology
U151	18.2	Central			15.4				Pyritic massive sulfide (sphalerite-galena bearing)
U151	16.4	Central			14.4				Sphalerite-galena bearing pyritic quartzite
U151	13.9	Central	14.44		14.1		14.3		Ribbon-banded graphitic, sulfidic quartzite (siliceous, sphalerite-galena bearing)
U151	11.3	Central			17.5				Ribbon-banded graphitic, sulfidic quartzite (siliceous, sphalerite-galena bearing)
U151	6.3	Central			16.1				Nonpyritic quartzite (sphalerite-galena bearing, carbonaceous)
U151	5.6	Central			16.4				Pyritic massive sulfide (sphalerite-galena bearing)
U151	1.8	Central			14.3	13.6			Pyritic massive sulfide (sphalerite-galena bearing)
U153	41.3	Central	35.36				15.6	29.5	Baritic massive sulfides (sphalerite-galena bearing)
U153	37.4	Central	27.40			12.2	12.9	28.0	Baritic massive sulfides (sphalerite-galena bearing)
U153	33.9	Central	30.57	11.0	19.2	18.7	18.1		Pyritic massive sulfide (siliceous, sphalerite-galena bearing)
U153	32.8	Central	26.16			14.8	14.6		Ribbon-banded graphitic, sulfidic quartzite (sphalerite-galena bearing)
U153	31.2	Central	37.00			15.9	16.0		Pyritic massive sulfide (sphalerite-galena bearing)
U153	29.8	Central	48.90		16.3		15.7		Pyritic massive sulfide
U153	27.8	Central	12.90	13.4	17.1	14.6	15.5		Ribbon-banded graphitic, sulfidic quartzite (siliceous, sphalerite-galena bearing)
U153	25.5	Central	35.69				16.1		Pyritic massive sulfide
U153	21.5	Central	8.73				16.0		Ribbon-banded graphitic, sulfidic quartzite (siliceous, sphalerite-galena bearing)
U153	19.0	Central	15.59			18.6	19.5		Ribbon-banded graphitic, sulfidic quartzite (siliceous, sphalerite-galena bearing)
U153	17.7	Central	29.87				23.1		Ribbon-banded graphitic, sulfidic quartzite (siliceous, fine-grained pyrite)
U153	8.8	Central	15.25			15.8	15.5		Ribbon-banded graphitic, sulfidic quartzite (siliceous, sphalerite-galena bearing)

[1] Depths arranged in proper statigraphic order
[2] Total sulfide
[3] Physically separated

Swim, two samples from Sea, and two samples from veins in the Anvil batholith. Samples from the Faro and Swim deposits were analyzed during both studies, allowing comparison of the two data sets. There is a small (about 0.1%) but consistent difference between LeCouter's average values for Faro and Swim and the averages determined in this study. The average values for the Sea and Vangorda deposits obtained by LeCouter (1973) have been normalized to the present data.

Sulfur Isotope Results

Geochemical and lithological data are summarized in Tables 3, 4, and 5 for mineralized samples. The range of $\delta^{34}S$ values of bulk sulfide is closely similar in the three deposits studied, with a general range

TABLE 5. Geochemical and Lithologic Data for the DY Deposit

Core no.	Depth (m)	Sulfide horizon[1]	% $C_{organic}$	%S_{total}	$\delta^{34}S$ (‰) GnSlPo[2]	Pyrite	Pyrrhotite[3]	Total S	Barite	Lithology
77-11	549.7–551.3	5		9.69						Massive sulfide
77-11	554.8–557.1	5	0.12	7.05	13.9	13.6		13.7		Carbonate-bearing, pyritic massive sulfide
77-11	557.1–558.2	5		14.71	13.1	13.8		13.6		Baritic massive sulfides (pyrrhotitic)
77-11	558.8–560.3	5	0.10	14.95	15.6	15.6	16.4	15.6		Pyritic quartzite (pyrrhotitic)
77-11	560.7–561.7	5	0.22	9.31				14.5		Ribbon-banded graphitic, sulfidic quartzite
77-11	561.7–563.7	5		39.46	13.3	15.7		15.6		Pyritic massive sulfide (baritic)
77-11	563.7–565.1	5	0.34	17.83	13.8	12.6		12.7		Pyritic quartzite
77-11	565.1–566.5	5	0.08	21.10	14.6	15.4		15.4		Pyritic quartzite
77-11	566.5–567.9	5	0.20	12.55	14.5	15.3		15.2		Pyritic quartzite
77-11	568.3–570.0	5	0.10	17.42	14.4	14.6		14.6		Ribbon-banded graphitic, sulfidic quartzite
77-11	570.3–571.6	5	0.13	18.68	15.2	17.6		17.4		Ribbon-banded graphitic, sulfidic quartzite
77-11	571.6–572.9	5	0.25	1.97				15.1		Vangorda unit: muscovite + chlorite ± biotite phyllite
77-11	572.9–574.0	5		13.99	18.6	16.3	16.4	16.9		Ribbon-banded graphitic, sulfidic quartzite
77-11	574.0–576.0	5	0.18	2.80	15.9	15.3	14.8	15.5		Vangorda unit: muscovite + chlorite ± biotite phyllite
77-11	576.0–577.0	5	0.13	3.94	14.6	14.0	14.3	14.4		Vangorda unit: muscovite + chlorite ± biotite phyllite
77-11	577.0–578.5	5	0.24	10.90	15.8	15.6	15.1	15.6		Vngorda unit: muscovite + chlorite ± biotite phyllite
77-11	578.5–580.5	5	0.16	13.91	15.9	15.7		15.7		Ribbon-banded graphitic, sulfidic quartzite
77-11	580.5–582.3	5	0.15	10.43	14.6	19.1		17.7		Ribbon-banded graphitic, sulfidic quartzite
77-11	582.3–584.3	5	0.02	3.03				15.8		Carbonate-bearing, pyritic massive sulfide
77-11	660.5–661.5	4		13.85				18.4		Pyritic quartzite (pyrrhotitic)
77-11	661.5–662.8	4		19.75	18.1	15.4	17.3	15.5		Pyritic quartzite (pyrrhotitic)
77-11	662.8–664.5	4		34.60	17.2	15.8		15.8		Pyritic massive sulfide (siliceous)

77-11	664.5–665.9	4	1.78	31.83	16.6	16.6	16.6		Pyritic massive sulfide (magnetite bearing)
77-11	665.9–667.8	4		30.03	15.9	15.6	15.7		Baritic massive sulfides (magnetite bearing)
77-11	667.8–669.3	4		24.30	16.0	15.1	15.1		Baritic massive sulfides (siliceous)
77-11	669.3–670.6	4		35.67	17.0	15.6	15.6		Baritic massive sulfides (magnetite bearing)
77-11	670.6–672.5	4		8.85			11.5		Baritic massive sulfides
77-11	673.8–675.7	4		34.55	12.1	13.7	13.6	21.3	Pyritic massive sulfide (magnetite bearing)
77-11	675.5–676.7	4	0.18	32.22	14.2	17.8	17.7	38.3	Pyritic massive sulfide
77-11	676.7–678.1	4	0.14	38.12	15.4	14.9	14.9		Pyritic massive sulfides (siliceous)
77-11	678.6–679.6	4	0.78	18.53	11.6	14.2	14.0	35.4	Pyritic massive sulfides (siliceous)
77-11	679.6–681.6	4	0.49	12.15	17.6	17.7	17.7		Ribbon-banded graphitic, sulfidic quartzite
77-11	681.6–683.3	4	0.65	14.78	18.4	19.4	19.3		Ribbon-banded graphitic, sulfidic quartzite
77-11	688.1–690.1	4	0.65	16.99	19.4	21.3	21.2		Ribbon-banded graphitic, sulfidic quartzite
77-11	690.1–691.1	4		40.34	19.1	16.3	16.3		Pyritic massive sulfide (siliceous)
77-11	691.1–692.7	4		27.94					Pyritic massive sulfide (siliceous)
77-11	731.2–732.2	3	0.09	37.10	16.0	15.4	15.4		Pyritic massive sulfide (siliceous)
77-11	769.6–771.6	2	0.48	14.48			14.9	34.3	Baritic massive sulfides
77-11	771.6–773.6	2	0.28	7.74	13.3	15.1	14.5		Ribbon-banded graphitic, sulfidic quartzite
77-11	773.6–775.6	2	0.30	9.13	12.4	13.6	13.3		Ribbon-banded graphitic, sulfidic quartzite
77-11	775.6–777.6	2	0.57	7.64	13.2	14.8	14.3		Ribbon-banded graphitic, sulfidic quartzite
77-11	777.6–779.6	2	0.61	11.69	16.2	21.6	39.5		Ribbon-banded graphitic, sulfidic quartzite
77-11	779.6–781.6	2	0.58	6.73			13.4		Ribbon-banded graphitic, sulfidic quartzite
77-11	781.6–783.6	2	0.49	7.62	13.5	14.6	28.1		Ribbon-banded graphitic, sulfidic quartzite
77-11	783.6–785.6	2	0.26	4.35	12.7	14.8	25.7		Ribbon-banded graphitic, sulfidic quartzite
77-11	785.6–787.6	2	0.34	1.43			12.5		Ribbon-banded graphitic, sulfidic quartzite
77-11	787.6–789.6	2	0.44	6.11	13.3	15.2	28.3		Ribbon-banded graphitic, sulfidic quartzite
77-11	789.6–791.7	2	0.85	4.83			14.8		Ribbon-banded graphitic, sulfidic quartzite
78-11	468.6–470.6	5		29.32			13.8		Pyritic massive sulfide (magnetite bearing)

TABLE 5—(*Cont.*)

Core no.	Depth (m)	Sulfide horizon[1]	% $C_{organic}$	%S_{total}	$\delta^{34}S$ (‰) GnSlPo[2]	Pyrite	Pyrrhotite[3]	Total S	Barite	Lithology
78-11	470.6–471.8	5	0.17	29.83				13.8		Pyritic massive sulfide (magnetite bearing)
78-11	471.8–473.8	5	0.17	27.35				14.1		Pyritic massive sulfide (magnetite bearing)
78-11	473.8–475.8	5		30.61				14.5		Pyritic massive sulfide (magnetite bearing)
78-11	475.8–477.8	5		27.85				14.1		Pyritic massive sulfide (magnetite bearing)
78-11	477.8–479.4	5		24.01				20.4		Pyritic massive sulfide (magnetite bearing)
78-11	550.2–552.2	4	2.43	6.09				17.8		Ribbon-banded graphitic, sulfidic quartzite
78-11	552.2–554.1	4	0.48	10.64				14.1		Ribbon-banded graphitic, sulfidic quartzite
78-11	554.1–556.2	4	1.00	5.26				15.3		Ribbon-banded graphitic, sulfidic quartzite
78-11	556.2–558.3	4	1.34	4.63						Ribbon-banded graphitic, sulfidic quartzite
78-11	558.3–560.1	4	0.95	4.04				14.7		Ribbon-banded graphitic, sulfidic quartzite
78-11	560.1–561.2	4	0.37	2.34				14.2		Ribbon-banded graphitic, sulfidic quartzite
78-11	561.2–562.3	4	0.39	4.47						Ribbon-banded graphitic, sulfidic quartzite
78-11	583.1–584.1	3	0.51	6.50				16.5		Ribbon-banded graphitic, sulfidic quartzite
78-11	584.1–586.1	3	2.46	8.26				15.8		Ribbon-banded graphitic, sulfidic quartzite
78-11	586.1–587.5	3	0.14	11.23				15.4		Ribbon-banded graphitic, sulfidic quartzite
78-11	587.5–589.5	3	0.31	1.51				14.0		Ribbon-banded graphitic, sulfidic quartzite
78-11	589.5–591.5	3		1.99				13.7		Ribbon-banded graphitic, sulfidic quartzite
78-11	591.5–592.5	3		2.79				13.3		Ribbon-banded graphitic, sulfidic quartzite
78-11	592.5–594.2	3	0.20	1.72				10.0		Ribbon-banded graphitic, sulfidic quartzite
78-11	607.3–609.3	3	5.98	6.24				14.5		Ribbon-banded graphitic, sulfidic quartzite
78-11	609.3–611.3	3	1.22	8.26				15.2		Ribbon-banded graphitic, sulfidic quartzite
78-11	611.3–613.3	3	5.23	9.96				14.1		Ribbon-banded graphitic, sulfidic quartzite

78-11	613.3–615.3	3	1.59	5.09			17.1		Ribbon-banded graphitic, sulfidic quartzite
78-11	615.3–617.2	3	1.05	11.27			15.9		Ribbon-banded graphitic, sulfidic quartzite
78-11	617.2–618.3	3	0.14	9.66			17.3		Pyritic massive sulfide
78-11	618.3–619.6	3	0.21	8.79			17.7	35.4	Baritic massive sulfides (sphalerite-galena bearing)
78-11	619.6–621.6	3		9.27			19.2		Sphalerite-galena bearing pyritic quartzite
78-11	621.6–623.6	3		18.68					Sphalerite-galena bearing pyritic quartzite
78-11	623.6–625.2	3		21.85					Sphalerite-galena bearing pyritic quartzite
78-11	625.2–627.2	3	0.60	22.61			13.9		Ribbon-banded graphitic, sulfidic quartzite
78-11	627.2–629.2	3	0.53	13.09			13.7		Ribbon-banded graphitic, sulfidic quartzite
78-11	629.2–631.2	3	0.05	19.63			13.6		Ribbon-banded graphitic, sulfidic quartzite
78-11	631.2–632.2	3	0.28	20.76			13.2		Ribbon-banded graphitic, sulfidic quartzite
78-11	632.2–634.1	3	0.10	14.36			16.1		Ribbon-banded graphitic, sulfidic quartzite
78-11	636.0–638.0	3	5.92	2.67			18.0		Vangorda unit: calcareous, graphitic phyllite (siliceous)
78-11	638.0–641.0	3	2.85	11.05			19.0		Ribbon-banded graphitic, sulfidic quartzite
79-07	574.2–576.1	4		26.07	17.4	18.8	18.7	41.5	Baritic massive sulfides
79-07	576.1–577.8	4		25.11	15.1	19.1	18.7	36.0	Baritic massive sulfides
79-07	577.8–578.6	4		39.70	14.9	13.3	13.7		Baritic massive sulfides
79-07	578.6–580.3	4	0.10	18.29	19.9	20.2	20.2		Sphalerite-galena bearing pyritic quartzite
79-07	580.3–581.4	4		15.91	22.4	22.4	22.4		Sphalerite-galena bearing pyritic quartzite
79-07	581.4–583.3	4	0.18	33.37	16.4	16.9	16.8		Pyritic massive sulfide (sphalerite-galena bearing)
79-07	583.0–582.2	4	0.15	2.61	18.4	19.8	19.5		Ribbon-banded graphitic, sulfidic quartzite (siliceous)
79-07	585.2–586.8	4		6.08	18.1	19.2	18.2		Ribbon-banded graphitic, sulfidic quartzite (siliceous)
79-09	580.2–582.2	4	0.41	6.17	14.2	15.9	15.2		Ribbon-banded graphitic, sulfidic quartzite (sphalerite-galena bearing)
79-09	582.2–584.2	4	0.31	7.63	17.0	18.8	18.3		Ribbon-banded graphitic, sulfidic quartzite (sphalerite-galena bearing)

TABLE 5—(*Cont.*)

Core no.	Depth (m)	Sulfide horizon[1]	% $C_{organic}$	$\%S_{total}$	$\delta^{34}S$ (‰)					Lithology
					CnSlPo[2]	Pyrite	Pyrrhotite[3]	Total S	Barite	
79-09	584.2–586.2	4	0.44	9.44	17.3	18.9		18.5		Ribbon-banded graphitic, sulfidic quartzite (sphalerite-galena bearing)
79-09	586.2–587.6	4	0.78	3.26	16.0	17.1		16.5		Ribbon-banded graphitic, sulfidic quartzite (sphalerite-galena bearing)
79-09	592.6–595.0	4	0.54	9.87	14.5	14.4		14.4		Ribbon-banded graphitic, sulfidic quartzite
79-09	597.2–597.9	4	0.45	8.14	13.3	12.9		13.1		Ribbon-banded graphitic, sulfidic quartzite
79-09	598.1–600.3	4	0.27	9.68	13.6	13.8		13.7		Ribbon-banded graphitic, sulfidic quartzite
79-09	600.3–602.5	4	0.15	4.92	15.2	15.8		15.6		Ribbon-banded graphitic, sulfidic quartzite
79-09	606.0–607.7	4		7.40	17.1	17.4		17.3		Carbonate-bearing, pyritic massive sulfide (sphalerite-galena bearing)
79-09	609.9–611.3	4	0.08	2.77	21.9	15.4		18.2		Carbonate-bearing, pyritic massive sulfide (sphalerite-galena bearing)
79-11	779.2–779.8	3	0.01	48.36	14.9	14.8		14.8		Pyritic massive sulfide (chalcopyrite bearing)
79-11	779.8–781.5	3	0.33	29.76	15.1	16.0		15.8		Baritic massive sulfides (sphalerite-galena bearing)
79-11	781.5–783.0	3		36.73	14.3	14.7		14.7		Baritic massive sulfides (sphalerite-galena bearing)
79-11	783.0–784.7	3		55.08	13.0	13.8		13.7		Baritic massive sulfide (sphalerite-galena bearing)
79-11	784.7–785.7	3		43.07	12.5	14.7		14.6		Nonpyritic massive sulfide (sphalerite-galena bearing)
79-11	785.7–787.2	3	0.32	41.61	14.9	14.5		14.6		Nonpyritic massive sulfide (sphalerite-galena bearing)
79-11	787.2–789.2	3	1.06	45.03	14.4	14.3		14.3		Nonpyritic massive sulfide (sphalerite-galena bearing)

79-11	789.2–790.7	3	0.22	23.36	14.5	20.1		18.7		Baritic massive sulfides (sphalerite-galena bearing)
79-11	790.7–792.3	3		46.99	11.3	15.2		15.0		Pyritic massive sulfide (magnetite bearing)
79-11	792.3–793.6	3		37.04	12.5	15.6		15.5		Pyritic massive sulfide (magnetite bearing)
79-11	793.6–795.0	3	0.06	19.07	15.9	18.0		17.4	35.8	Bartic massive sulfides (sphalerite-galena bearing)
79-11	795.0–796.2	3	0.07	20.10	16.1	16.9		16.6		Baritic massive sulfide (sphalerite-galena bearing)
79-11	796.2–797.7	3	0.08	40.36	17.6	19.3		19.2		Sphalerite-galena bearing pyritic quartzite
79-11	797.7–799.7	3	0.02	16.27	16.3	16.2		16.2		Sphalerite-galena bearing pyritic quartzite (pyrrhotitic)
79-11	799.7–801.7	3		21.84	16.2	15.2		15.3		Sphalerite-galena bearing pyritic quartzite (pyrrhotitic)
79-11	801.7–802.9	3		16.63	15.7	16.9	15.8	16.2		Sphalerite-galena bearing pyritic quartzite (pyrrhotitic)
79-11	802.9–804.3	3	0.12	12.63	14.1	15.0		14.8		Sphalerite-galena bearing pyritic quartzite (phyrrhotitic)
79-12	723.8–724.4	3	0.73	35.36	14.7	14.3		14.4		Pyritic massive sulfide (siliceous)
79-12	724.4–725.0	3		25.25	17.1	19.8		19.4	38.6	Baritic massive sulfides (sphalerite-galena bearing)
79-12	725.0–727.0	3		20.39	16.9	17.2		17.2	26.7	Baritic massive sulfides (sphalerite-galena bearing)
79-12	727.0–729.0	3		29.30	16.2	16.6		16.5		Baritic massive sulfides (sphalerite-galena bearing)
79-12	729.0–730.0	3		12.17	17.4	17.7		17.6	22.8	Baritic massive sulfides (sphalerite-galena bearing)
79-12	730.0–732.3	3	0.32	19.79	16.3	17.4		17.2		Baritic massive sulfides (sphalerite-galena bearing)
79-12	732.3–733.5	3	0.22	19.79	16.4	20.7		19.7	22.7	Baritic massive sulfides (sphalerite-galena bearing)
79-12	733.5–735.0	3	0.38	17.29	17.2	18.6		18.1	23.3	Sphalerite-galena bearing pyritic quartzite
79-12	735.0–736.1	3		39.45	14.8	14.9		14.9		Pyritic massive sulfide (magnetite bearing)
79-12	736.1–737.3	3		8.71	16.3	17.7		17.4		Baritic massive sulfide (sphalerite-galena bearing)

TABLE 5—(*Cont.*)

Core no.	Depth (m)	Sulfide horizon[1]	% $C_{organic}$	$\%S_{total}$	$\delta^{34}S$ (‰) GnSlPo[2]	Pyrite	Pyrrhotite[3]	Total S	Barite	Lithology
79-12	737.3–737.7	3		27.39	17.8	17.7		17.7		Pyritic massive sulfide (sphalerite-galena bearing)
79-12	737.7–738.8	3	0.40	14.12	16.3	17.7		17.5		Nonpyritic massive sulfide (siliceous)
79-12	738.8–740.8	3		21.37	16.1	17.6		17.5		Pyritic quartzite
79-12	740.8–743.1	3	0.07	19.09	15.9	16.6		16.5		Pyritic quartzite
79-12	743.1–745.1	3	0.03	19.27	14.5	14.8		14.8		Pyritic quartzite (pyrrhotitic)
79-12	745.1–746.0	3	0.08	28.32	12.8	13.5	12.4	13.4		Pyritic quartzite (pyrrhotitic)
79-12	746.0–747.0	3	0.10	33.54	12.6	12.6		12.6		Pyritic quartzite (magnetite bearing)
79-12	747.0–749.5	3	0.60	13.71	15.4	15.4		15.4		Ribbon-banded graphitic, sulfidic quartzite (chalcopyrite bearing)

[1] Refer to Figure 4 for horizon numbers and Figures 4 and 9 for drill hole locations
[2] SlGnPo = sphalerite + galena ± pyrrhotite, extracted in 6 *N*, 60°C HCl
[3] Physically separated pyrrhotite

from 10 to 22 per mil (Fig. 7). Sulfur isotope ratio values of sulfides from unmineralized Anvil Range samples (Table 2, Fig. 7) are broadly similar to mineralized samples but cover a wider range, extending from 5 to 35 per mil.

Barite was studied from all three deposits and shows remarkable isotopic variation (Fig. 7). In DDH 66-52 from the Faro deposit, barite has quite uniform values centered about 24 per mil. In contrast, barite values for the Grum deposit cluster near 31 per mil and in the DY deposit they range from 21 to 42 per mil, with some indication of bimodality.

Faro deposit

Samples from only a single drill hole through the Faro deposit were analyzed, because Campbell and Ethier (1974) previously studied the deposit. The particular hole selected (Fig. 4) has a reasonably well developed Anvil cycle in the mineralized intersection (Table 3), which was carefully sampled. Much of the massive sulfide in this intersection is recrystallized to coarse-grained "buckshot" ore with 1- to 5-mm pyrite porphyroblasts.

The $\delta^{34}S$ values of bulk sulfide in the Anvil cycle of drill hole 66-52 show a marked upward increase of about 4 per mil (Fig. 8). Most of these samples are from the buckshot massive sulfide facies, yet significant and systematic stratigraphic variation in $\delta^{34}S$ values is preserved, indicating that metamorphic sulfur isotope reequilibration occurs only on a grain to grain basis and is not important in a macroscopic sense.

Grum deposit

Eleven surface and underground drill holes from the Grum deposit were selected for structural, lithologic, petrographic, and sulfur isotope studies. Details of the results are available in Modene (1982).

The multiple sulfide lenses of the Grum deposit (Fig. 5) are in direct contrast to the single-layered nature of the Faro deposit. Variation in wall-rock lithologies and, hence, stratigraphic positions preclude the possibility that the three main massive sulfide horizons at Grum are simply a refold of a single horizon. Anvil cycles are well developed in the central massive horizon (Table 4, holes A24 and U153), but all Grum horizons show preferential development of the distal ribbon-banded facies relative to Faro.

Variations in $\delta^{34}S$ values within the Grum horizons do not consistently show the systematic upward increase in $\delta^{34}S$ values of hole 66-52 from the Faro deposit (Table 4; Modene, 1982). However, upward (stratigraphically) increasing $\delta^{34}S$ values and well-developed Anvil cycles occur concurrently in holes A109 and U142 (Table 4).

Sulfur isotope geothermometry was attempted using sulfide minerals separated by hand picking samples from the Grum deposit (Table 4). Coexisting

TABLE 6. Lead Isotope Data for Anvil Range Deposits

Deposit	Core	Depth (m)	$^{206}Pb/^{204}Pb$	$^{207}Pb/^{204}Pb$	$^{208}Pb/^{204}Pb$	$\delta^{34}S$ (‰)
DY	77-11	549.7	18.379	15.591	38.195	
		571.6	18.411	15.650	38.331	15.1
		582.3	18.396	15.658	38.515	15.8
		660.5	18.411	15.685	38.384	18.4
		670.6	18.383	15.660	38.337	11.5
		769.6	18.431	15.676	38.377	14.9
		779.6	18.431	15.644	38.384	13.4
		789.6	18.419	15.610	38.321	14.8
DY	78-11	464.9	18.386	15.665	38.241	
		477.8	18.376	15.643	38.335	17.8
		554.1	18.451	15.656	38.539	15.3
		556.2	18.390	15.628	38.306	
		561.2	18.411	15.672	38.464	
		583.1	18.407	15.661	38.193	16.5
		586.1	18.404	15.599	38.268	15.4
		592.5	18.403	15.648	38.415	10.0
		607.3	18.389	15.650	38.404	14.5
		618.3	18.417	15.648	38.337	17.7
		615.3	18.389	15.633	38.304	15.9
		621.6	18.424	15.655	38.326	
		636.0	18.473	15.662	38.483	18.0
Faro	66-52	165.7	18.342	15.625	38.290	16.2
		178.7	18.316	15.645	38.205	19.1
		189.1	18.414	15.674	38.364	14.8
Grum grab sample			18.846	15.717	38.899	
	A135	52.0	18.446	15.688	38.607	
		80.0	18.409	15.646	38.291	
		143.0	18.405	15.686	38.347	
	U21	15.0	18.401	15.691	38.227	
		41.0	18.375	15.642	38.320	
	U10	10.0	18.479	15.711	38.383	
	U72	125.0	18.403	15.643	38.342	
Swim	A25	101.9	18.337	15.649	38.299	
	A35	111.7	18.327	15.624	38.136	
SB	74-04	131.5	18.530	15.655	38.397	
	74-03	76.3	18.370	15.678	38.394	
	456-75-03	260.2	18.586	15.670	38.783	
	456-75-04	126.3	18.436	15.673	38.426	

sphalerite, galena, and pyrite separates were obtained from four samples, and additional single mineral pairs were obtained from several other samples. However, temperatures computed from the three possible mineral pairs in each of the samples are randomly discordant and give a temperature range from 178° to 541°C (Modene, 1982). Moreover, consistent isotopic temperatures were not obtained from any single mineral pair (e.g., sphalerite-galena). In general, ^{34}S is enriched in the expected order (pyrite > sphalerite > galena), but the fractionation is often small, giving impossibly high temperatures, and in some cases, there are reversals.

In contrast, Campbell and Ethier (1974) obtained reasonably consistent isotopic temperatures, averaging 306°C, for pyrite-galena pairs in the Faro orebody. Campbell and Ethier (1974) suggest that this temperature represents the point at which isotopic equilibration ceased during cooling from the amphibolite facies metamorphism caused by Anvil batholith intrusion. Apparently, Anvil Range sulfides did not form in primary sulfur isotope equilibrium, and deposits which were subjected only to lower greenschist metamorphism (DY, Grum) did not experience grain to grain isotopic reequilibration of sulfide minerals.

DY deposit

Six holes from the DY deposit were selected for study, and two of these, 78-11 and 77-11 (Fig. 4b), were sampled in detail. The DY deposit, like Grum, consists of intensely deformed multiple sulfide lenses (Fig. 4b); the detailed geometry of individual lenses is poorly understood. Anvil cycles in the DY deposit often are poorly developed or truncated by other

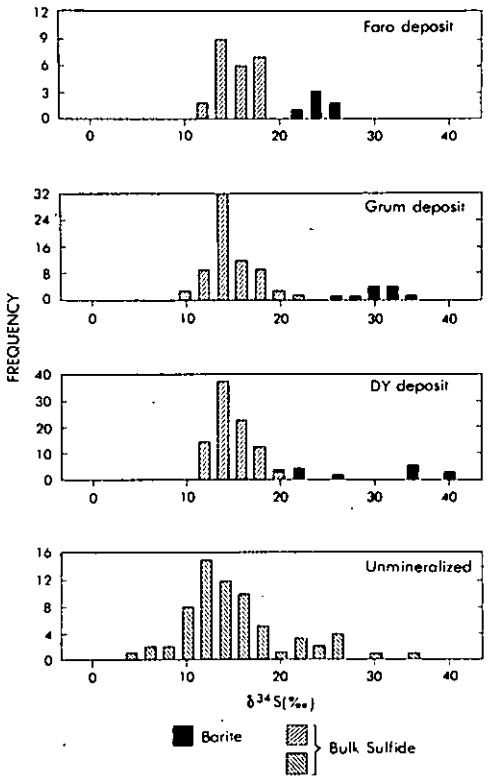

FIG. 7. Sulfur isotope distributions of bulk sulfide and barite from the Faro, Grum, and DY deposits and unmineralized Anvil Range samples. Close overlap in sulfide values indicates similar sulfur sources for all samples. The $\delta^{34}S$ values of barite samples vary considerably between deposits, probably due to variations in ore fluid-bottom water mixing at the depositional site. See Tables 2, 3, 4, and 5 for detailed geochemical and lithologic data.

subcycles (Table 5). Some of the truncation undoubtably is due to structural repetition. However, the major intersections (horizons 5, 4, and 3; Fig. 4b) are not refolds of a major sulfide horizon because they occur in distinctly different host lithologies (Fig. 4b).

Vertical variations in $\delta^{34}S$ values within individual intersections from the DY deposit are often nonsystematic, as is Anvil cycle development. In general, there are no mineralized intersections in any of the studied DY holes which show simple upward development of the idealized Anvil cycle (Fig. 6). Examination of data in Table 5 indicates that the best cycles are developed in holes 78-11 (632–620 m), 79-11 (803–795 m), and 79-07 (585–573 m). The $\delta^{34}S$ values show systematic upward increases in the 78-11 and 79-11 Anvil cycles but large random variations in 79-07, which has intercalations of host lithologies and redevelopment of the ribbon-banded graphitic sulfide unit at the top. Horizons 4 and 5 in hole 77-11 show a general upward conformity to Anvil cycle lithologic variations, but there are many reversals and intercalations of host lithologies. The $\delta^{34}S$ values do not show systematic variation in these intersections.

In contrast, lateral within-deposit variations in $\delta^{34}S$ values are shown by decreasing average values and ranges away from drill hole 79-07 (in the northeastern portion of the deposit) toward the south and southwest, over a horizontal distance of nearly 700 m (Fig. 9). The stronger development of white mica alteration in the southwestern portion of the DY deposit is coincident with lighter $\delta^{34}S$ values, which may indicate proximity to the exhalative center.

An unusual feature of the DY deposit is the presence of numerous banded and massive (sometimes spotted) chloritic units interlayered with and immediately northeast of the deposit. These units are interpreted as metamorphosed mafic sills, flows, and tuffs. Despite the abundance of metabasaltic material closely associated with mineralization in the DY deposit, the range and mean of the $\delta^{34}S$ values for DY samples are very similar to Faro and Grum, suggesting that basaltic sulfur contributions, if present, are not related to spatial proximity of volcanic material.

Discussion

Regional depositional environment

Large (1980) has suggested that many sedimentary exhalative Pb-Zn deposits can be described in terms of localization within first-, second-, and third-order basins. First-order basins have broad regional significance, second-order basins often have district-level significance, and third-order basins represent the actual depocenter of massive sulfide formation. This classification allows convenient separation of regional, local, and hydrothermal sedimentary effects.

The first-order basin which includes the Anvil district is, of course, the Selwyn basin (Fig. 1). The Selwyn basin accumulated clastic sediments during much of the late Proterozoic and Paleozoic, as the northern cordillera evolved following a Wilson cycle (see Monger and Price, 1979; Tempelman-Kluit, 1979, for re-

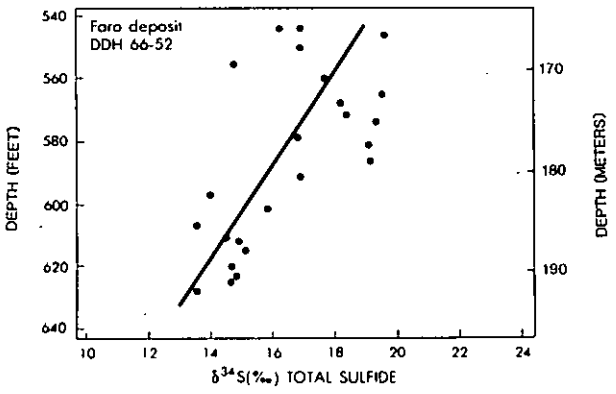

FIG. 8. Sulfur isotope variation in bulk sulfide samples from drill hole 66-52, Faro deposit. Shows upward-increasing $\delta^{34}S$ values in a well-developed Anvil cycle. Correlation coefficient ($r^2 = 0.64$) based on linear regression.

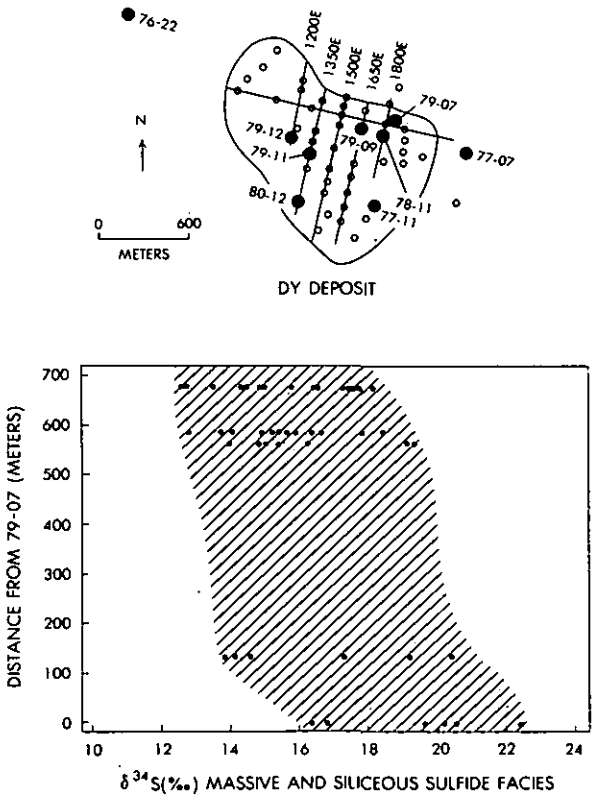

FIG. 9. Drill-hole collar locations and lateral bulk sulfide sulfur isotopic variations in DY deposit mineralized samples. Numbered holes are those used in this study. Deposit outline is projected to the surface. The $\delta^{34}S$ values show a general decrease away from drill hole 79-07 toward the southwest portion of the deposit. White mica alteration also is better developed in the southwestern portion of the deposit (Fig. 4b), indicating a possible ore fluid vent area.

cent models of cordilleran evolution). Therefore, by inference, the Anvil district may be underlain by red beds and evaporites deposited in the incipient rift basin on Proterozoic continental crust. These postulated shallow marine and continental deposits may have been overlain, as the rift basin deepened, by thick, relatively coarse turbidites. If subsidence out-paced sedimentation, the coarse clastics would grade upward to finer sediments, ultimately to be capped by deep-water shales. The Mt. Mye unit may represent the shale-rich upper part of this hypothesized stratigraphic cycle. The Grit unit of the Windemere Supergroup (Gabrielse et al., 1973), which presumably extends beneath the Mt. Mye unit in the Anvil district, may be the upper part of the turbidite package. Deeper in the section there may be Hadrynian evaporites and arkosic rocks which were important salinity and metal sources. Alternatively, older evaporite-red bed sequences of the Purcell Supergroup in the Mackenzie Mountains (Eisbacher, 1980) may extend beneath the Selwyn basin to the Anvil area.

Thus, the Selwyn basin may have existed as an epicratonic trough in the contemporaneous continental margin and may be bounded by fault-controlled hinge zones. Block faulting along such hinge zones often produces restricted second-order basins with lateral dimensions which can be measured in tens of kilometers. Such basins are characterized by rapid vertical and lateral facies variations. For example, Mako and Shanks (1984) describe the mineralized Vulcan occurrence in such a setting on the eastern margin of the Selwyn basin, at the transition to carbonates of the MacKenzie platform.

In the Anvil district, complex deformation and intrusion of the Anvil batholith (Fig. 2) have obscured direct evidence of geometric factors related to a possible second-order basin. However, the Anvil deposits thus far discovered occur along a curvilinear trend 35 km long. The deposits are localized in the stratigraphic transition zone between Mt. Mye metapelites and Vangorda calcareous pelites. More importantly, the deposits occur along the northeastern margin of an area of development of graphitic phyllite with thicknesses far in excess of that developed regionally in the Mt. Mye-Vangorda transition zone (Fig. 3). These observations, taken together, suggest the existence of a second-order basin which accumulated fine-grained, sometimes carbonaceous sediments and was, in general, a favorable environment for massive sulfide development. Faulting along the deposit hinge line may have provided pathways for ore fluid egress to the sea floor.

Third-order basins, with lateral dimensions equal to or slightly larger than the massive sulfides, probably also existed. The graphitic phyllite units tend to occur in lenses a few meters to tens of meters thick, with lateral dimensions of tens to hundreds of meters. Intimate association of graphitic lenses with massive sulfides strongly suggests a common restriction to third-order basins.

The unmineralized samples analyzed in this study (Table 2 and Fig. 2) are broadly representative of conditions at the time of ore formation. Conditions in the basin are of particular interest in relation to the mode of massive sulfide formation. Was the basin which hosted the Anvil deposits a restricted anoxic basin like the Black Sea (Ross and Degens, 1974) or a more open, periodically oxygenated area like the Santa Barbara basin (Emery, 1960)? Sulfur isotope distributions and sulfide sulfur and organic carbon contents provide useful information of relevance to this question. A number of studies (Berner, 1964; Hartmann and Nielsen, 1969; Goldhaber and Kaplan, 1974; Williams, 1978) have shown a general correlation between sulfide sulfur and organic carbon content in recent and ancient anaerobic marine sediments which contain iron sulfides derived from bacterial reduction of pore water sulfate. Moreover, Leventhal (1983) has shown that in the Black Sea the intercept of the S/C correlation line for recent, surficial sedi-

ments is elevated from the origin to positive sulfide sulfur values due to incorporation of sulfides precipitated in the water column.

The sulfur-carbon distribution for unmineralized Anvil Range samples (Fig. 10) is similar to Holocene Black Sea sediments, with most samples enriched in sulfur with respect to recent anaerobic sediments. However, there is significant scatter (Fig. 10), perhaps because many of the Anvil Range samples are not time-equivalent and may differ in age by millions of years. Conditions in the basin probably varied widely during the time interval sampled, with periodic variations in the degree of oxygenation and, conversely, water column sulfide production.

The $\delta^{34}S$ distributions (Fig. 7) indicate that unmineralized Anvil Range samples have values ranging from 5 to 34 per mil. Most Early Cambrian seawater sulfate ranged from 27 to 35 per mil (Claypool et al., 1980), tending to the heavier part of that range in the earliest Cambrian. Thus, the isotopic values of sulfides in the unmineralized samples range from much lighter than, to almost identical with, contemporaneous seawater sulfate. This distribution is consistent with closed system bacterial sulfate reduction (Schwarcz and Burnie, 1973; Jorgensen, 1979) and is similar to the range (10–20‰) of sulfides in sapropelic Black Sea sediments produced during neoeuxinian events (Vinogradov et al., 1962; Migdisov et al., 1974). However, the neoeuxinian period of Black Sea sedimentation was characterized by increased fresh-water input and increased restriction of seawater input. Thus, reduced sulfate supply results in isotopically heavy diagenetic sulfide minerals as seen in many occurrences of reducing nonmarine sediments (Cole and Picard, 1981). Similar heavy isotope ranges also have been found in sapropels interbedded with Miocene evaporites in the Red Sea (Shanks et al., 1973), but they are attributed to diagenetic reactions with continued sulfate supply from anhydrite in adjacent evaporites.

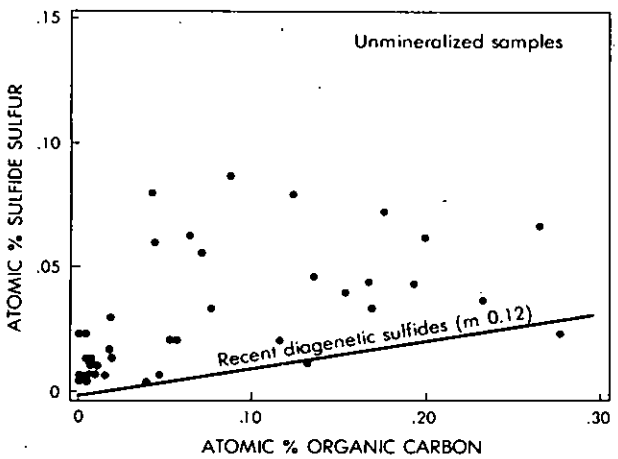

FIG. 10. Plot of noncarbonate (organic) carbon versus total sulfide sulfur for unmineralized Anvil Range samples. Solid line is general correlation line for recent bacteriogenic iron sulfides. Relatively high sulfide/organic carbon ratios of Anvil Range samples indicate excess sulfide contributed to the sediments due to precipitation in anoxic bottom waters. See text for discussion.

Neither fresh-water conditions nor extreme reduction during late diagenesis seem particularly applicable to the Anvil Range sulfides. Direct evidence is lacking for the salinity of the waters from which the Anvil Range sediments were deposited, due to the destruction of any possible fossil evidence by metamorphism and deformation. However, the presumed correlative units to the east, discussed earlier, contain marine fossils; much of the Selwyn basin was open to marine influence in the Early to Middle Cambrian. In addition, Goodfellow and Jonasson (1986) have documented marine conditions during the Lower Silurian stagnation event which coincides with formation of the Howards Pass deposit. Formation of the sulfide in the unmineralized Anvil Range metapelites by diagenetic reduction can be ruled out based on sulfur-carbon relationships (Fig. 10). Thus, we conclude that the sulfides in unmineralized Anvil Range samples formed by closed system bacterial sulfate reduction in an anoxic restricted basin. The anomalously high S/C ratios in these samples are due to water column sulfide production. Furthermore, the water column sulfide was derived from normal marine processes related to water column stagnation. Venting hydrothermal fluids did not contribute significant amounts of sulfide to the unmineralized Anvil Range sediments, as evidenced by the lack of relationship between sulfide sulfur content and sulfur isotope values (Table 2).

Did the closed system sulfate reduction which produced the $\delta^{34}S$ ranges in the unmineralized Anvil samples occur locally in the inferred second-order basin or was it a first-order phenomenon encompassing the entire Selwyn basin? Goodfellow and Jonasson (1984) have recently published sulfur isotope data on sedimentary pyrite samples from a variety of lithologies in the Selwyn basin which include an age range from Late Cambrian to Early Mississippian (Fig. 11). They find striking and compelling evidence for closed system sulfate reduction related to stagnation events in Early Silurian, Early Devonian, and Late-Middle Devonian; that is, they find sulfide $\delta^{34}S$ values which approach the contemporaneous seawater sulfate curve. If their samples are sufficiently remote from exhalative centers to be representative of the basin as a whole, then they have delineated a series of major geochemical events, with major exploration significance. Most likely, though, the Selwyn basin evolved with a density-stratified water column like the Black Sea (Deuser, 1974), with anoxic conditions in the deepest or most restricted parts of the basin. In the Selwyn basin, these may have been fault-bounded,

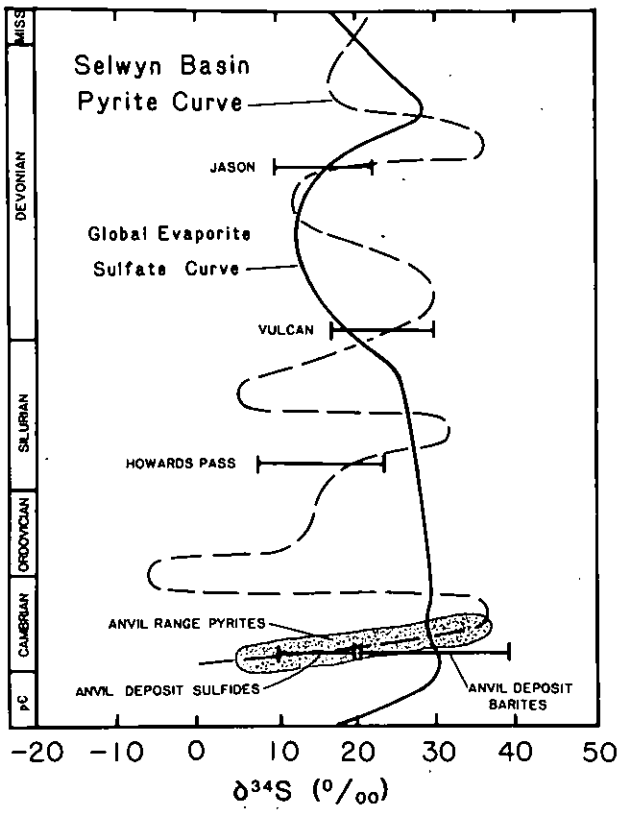

FIG. 11. Sulfur isotope age curves for pyrite and barite from the Selwyn basin (after Goodfellow and Jonasson, 1984) with Early Cambrian data from this study. Four early Paleozoic stagnation events are indicated by sedimentary pyrite $\delta^{34}S$ values which approach and in some cases exceed the global seawater sulfate curve of Claypool et al. (1980). Stratiform lead-zinc deposits are related to the onset of each of these anoxic events. Sulfur isotope data for the Jason deposit from Gardner and Hutcheon (1985), for the Vulcan deposit (Mako and Shanks, 1984), for Howards Pass (Goodfellow and Jonasson, 1986), and for Anvil (this study).

possibly silled, second-order subbasins of district-scale significance.

Detailed examination of stratigraphic variations in $\delta^{34}S$ values of sulfides in unmineralized samples from the DY deposit area indicates systematic upward increase from values of 10 to 26 per mil (Fig. 12). Such trends may be representative of stagnation cycles. Sulfur isotope data for DY deposit mineralized samples (Fig. 12) fall on this trend; they are a normal consequence of sulfur isotope evolution due to extensive sulfate reduction in the water column.

Comparison of the Anvil Range data for unmineralized samples with the sedimentary pyrite curve of Goodfellow and Jonasson (1984) confirms another stagnation event in the Early to Middle Cambrian (Fig. 11). Hence, the Anvil deposits formed during a period of closed system sulfate reduction which affected at least the area of the Anvil district and perhaps much of the Selwyn basin. However, additional work on Cambrian samples from other parts of the basin would be required to establish the areal extent of this stagnation cycle.

More importantly, the correlation of $\delta^{34}S$ values of ore deposits to the Selwyn basin sedimentary pyrite curve (Fig. 11) indicates that the major sediment-hosted lead-zinc deposits formed during stagnation events and that their $\delta^{34}S$ ranges are a result of processes active in the anoxic basin. This implies that the bulk of the sulfide in the ore deposits is derived from the water column, not from exotic ore fluids. Stratiform barite deposits in the Selwyn basin have $\delta^{34}S$ values which are consistent with this conclusion; most are heavier than contemporaneous seawater sulfate (Goodfellow and Jonasson, 1984).

Exhalative environment

Metamorphic textures developed in the Anvil Range ores leave no doubt that the ore minerals were formed prior to metamorphism. Well-developed ore mineral banding, interlayering with unmineralized metasedimentary rocks, the occurrence of the deposits in a curvilinear spatial array, the restriction to a narrow stratigraphic interval, and the association with graphitic facies all strongly suggest that the deposits are synsedimentary or syndiagenetic. The existence and nature of the Anvil cycles, particularly truncated cycles and multiply stacked mineralized lenses, also is indicative of sedimentary rather than epigenetic (postlithification) processes. A recurrently evolving set of environmental parameters at the site of sulfide deposition or in the area of hydrothermal fluid generation must be responsible for the Anvil cycles.

What was the nature of the depositional site of massive sulfide precipitation and accumulation? Wall-rock alteration developed around the deposits suggests that a hot saline fluid was involved in ore transport. Fluid inclusion work by Kuo (1976) on the Faro, Grum, and Swim Lakes deposits demonstrated that primary liquid-rich two-phase inclusions in barite and quartz give filling temperatures from 168° to 255°C and salinities from 3.6 to 9.2 equiv wt percent NaCl. Although these data must be interpreted with a great deal of skepticism due to the metamorphic and structural history of these deposits, it is interesting that the calculated densities of the fluids (0.83–0.93 g/cc) are all less than seawater. Taken at face value these data suggest that the Anvil deposits formed from dilute aqueous brines which, upon venting at the sea floor at 200° to 250°C, would have formed buoyant plumes in the water column. Interestingly, Gardner and Hutcheon (1985) have reported similar fluid inclusion data (T = 250°C; NaCl equiv = 9%) for the Jason deposit, at MacMillan Pass (Fig. 1).

The curvilinear array of deposits may indicate a synsedimentary fault or fault zone controlling basin topography, possibly providing topographic depres-

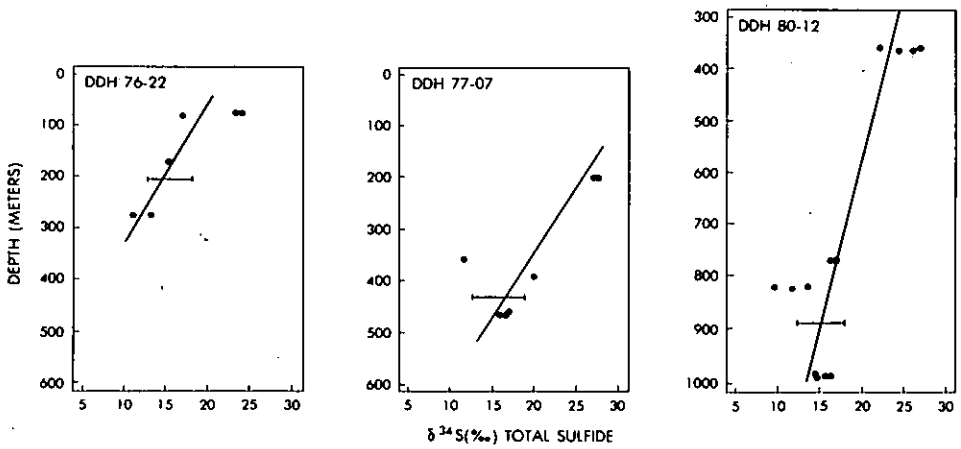

FIG. 12. Stratigraphic variation of $\delta^{34}S$ values of unmineralized samples from drill holes near the DY deposit. Range bars indicate the sulfur isotope range and approximate stratigraphic location of DY deposit sulfides. These data suggest a causal link between sulfide evolution in the basin and the formation of the DY deposit.

sions for localization of initially buoyant hydrothermal fluids. In addition, the presumed synsedimentary fault zone may have influenced sedimentary facies, particularly the zero edge of the deposit-associated graphitic phyllite. Fault or hinge lines may have provided channelways for hot subsurface fluid migration to the seawater-sediment interface. The predeformation geometry of the Anvil range deposits, tens of meters thick by hundreds of meters in lateral extent, can be described as sheetlike. This is more typical of deposits formed from supersaline brines which pool in seafloor deeps, but sheetlike deposits also can result from spreading plumes if the rate of sedimentation of the freshly precipitated minerals exceeds dispersion by bottom currents. Stratified third-order basins might provide a protected environment suitable for containment of such mineral precipitates.

Chemical evolution of the ore fluid, to produce the spatial arrangement of the facies in the Anvil cycle, is consistent with venting into an anoxic basin and localization in third-order basins. Anoxic conditions are conducive to preservation of the carbonaceous material in the ribbon-banded graphitic sulfide facies and in the unmineralized graphitic phyllite. The lensoidal nature of the deposit-associated graphitic phyllite zones was cited above as primary evidence for the existence of third-order basins in the Anvil Range, but are the strongly reducing conditions restricted to these deposit depocenters?

The lack of hanging-wall iron and manganese oxide or siliceous oxide deposits is distinct compared to many massive sulfide deposits (Franklin et al., 1981; Gustafson and Williams, 1981) and also provides indirect evidence on the extent of anoxic conditions. For example, the present-day Atlantis II Deep in the Red Sea represents an anoxic brine pool, but oxic conditions currently prevail in the Red Sea deep water, and admixture into the upper brine layer results in iron and manganese oxide "bathtub rings" around the brine deep. In addition, significant incorporation of oxides into the deposit occurs by sedimentation into the pool (Hartmann, 1973). Thus, it seems likely that anoxic conditions must have prevailed over fairly large areas in the Anvil Range, as concluded previously from S/C ratios and $\delta^{34}S$ values of sulfides in unmineralized samples.

The common occurrence of a baritic massive sulfide facies capping Anvil cycles, however, indicates the presence of dissolved sulfate in the ore fluid or in the anoxic seawater of the basin, or both. The $\delta^{34}S$ evidence (Fig. 7) bears directly on the origin of the barite, and on bottom-water conditions at the times of barite formation. Barites from the Grum deposit have $\delta^{34}S$ values which range from 28 to 35 per mil. The few Faro barites analyzed fall in the range 23 to 27 per mil. Barites from the DY deposit have $\delta^{34}S$ values which range from 21 to 42 per mil.

A possible explanation of the barite $\delta^{34}S$ data involves a dual sulfate source: Proterozoic evaporite sulfate (18–20‰) is carried in the ore fluid and residual marine sulfate in bottom water (30–60‰) is admixed at the site of deposit formation. Bottom-water sulfate might have $\delta^{34}S$ values ranging from that typical of Early Cambrian seawater (30‰) to very much heavier residual sulfate, depending on the intensity of the stagnation event at the time of ore precipitation. Of course, the concentration of sulfate in the bottom waters decreases progressively as sulfate reduction and the attendant isotope enrichment of sulfate proceeds. The effect can be modeled simply using the Rayleigh distillation equation (Broecker and Oversby, 1971):

$$\delta^{34}S = 1{,}000\,(1 - f^{\alpha-1}), \quad (1)$$

where δ is the per mil (‰) difference in the sulfur isotope values between initial sulfate and residual sulfate, f is the fraction of unreduced sulfate remaining, and α is the instantaneous fractionation factor for the sulfate reduction process. Laboratory experiments have shown that fractionation factors during bacterial sulfate reduction can range from approximately 1.025 to 1.050 (Kaplan, 1975), depending on the rate of reduction and the metabolic pathway utilized. Measured fractionation factors for marine sediments fall within the same range (Goldhaber and Kaplan, 1974), whereas fractionations of 1.050 or larger occur in the modern Black Sea water column (Sweeney and Kaplan, 1980). The $\delta^{34}S$ values of sulfide minerals in the Anvil deposits range from 10 to 22 per mil. Using a fractionation factor of 1.025, 20 to 50 percent of the water column sulfate must be reduced to give sulfide with the proper isotopic values; the residual sulfate values would range from 35 to 47 per mil. Using 1.050 requires 45 to 60 percent reduction, and gives residual sulfate at 60 to 75 per mil.

Whichever fractionation factor is used, the $\delta^{34}S$ values of the Anvil range barites can be explained by the two-component model presented above. The observation of barite as light as 21 per mil requires a source other than Cambrian seawater sulfate; late Proterozoic evaporite sulfates are close to this value (Claypool et al., 1980). Isotopically heavy barite, up to 42 per mil, requires a source heavier than Early Cambrian seawater sulfate. Residual sulfate following sulfate reduction in a system not replenished by open-ocean sulfate is implicated; Selwyn basin stagnation events record such a system.

Solubility considerations generally are consistent with the proposed origins of the baritic facies. Barite exhibits prograde solubility behavior in brines with greater than 1 *m* (5.9 wt %) NaCl, and simple cooling of a barite-saturated brine from 250° to 100°C can result in precipitation of 70 percent of the dissolved barium sulfate (Holland and Malinin, 1979). However, barite is less common in the graphitic, siliceous, and massive sulfide facies of the Anvil deposits, suggesting that the initial ore fluid is undersaturated with barite, probably due to relatively low sulfate concentrations. Barite solubility in a 1 *m* NaCl solution is approximately 120 ppm (Blount, 1977). Low sulfate concentration in the heated ore-forming brine is also consistent with anhydrite solubility relations; anhydrite, unlike barite, exhibits retrograde solubility behavior even in concentrated brines. The ore fluid probably carried substantially more calcium than barium, hence, anhydrite solubility at high temperatures limited sulfate to low values in the fluid. Much of the barite formed during mixing with bottom waters which, though depleted in sulfate by anoxic events, may still have contained more than 1,000 ppm. Thus, a relatively small amount of mixing of bottom water into ore fluid could have a substantial effect on barite precipitation and on the $\delta^{34}S$ value of the resultant barite.

The stacked multiple sulfide lenses of the Grum and DY deposits encompass significant stratigraphic intervals. Estimates based on assumed sedimentation rates (10 cm/1,000 yr) indicate that sulfide may have accumulated sporadically over an approximately 1.5-m.y. period (Jennings and Jilson, 1986). It is, thus, not unexpected that barite formation by mixing at the depositional site would respond to periodic changes in bottom-water and brine-venting conditions. Dramatic variations are known over much shorter time periods (15,000 yr) in the Atlantis II Deep, Red Sea (Shanks and Bischoff, 1980). However, the relatively narrow range of sulfur isotope values of sulfide minerals in the Anvil deposits confirms the basic constancy of sulfide source and transport processes.

The gradual increase in $\delta^{34}S$ values of sulfides upward through the Faro deposit Anvil cycle (Fig. 8) and laterally away from the source area for the DY sulfide horizons (Fig. 9) may be an indication of dual sulfide sources. The observed increase in average $\delta^{34}S$ values of approximately 4 per mil occurs at Faro over a stratigraphic interval of less than 30 m (Fig. 8). Hence, the variation is very sharp in comparison to the stratigraphic trend in $\delta^{34}S$ values documented for unmineralized samples from the DY area (Fig. 12) and probably is not due to sulfate reduction cycles in the water column. Most likely the ore fluid carries a small amount of light sulfide, perhaps from subsurface interaction with heat-generating mafic igneous rocks. Mixing with the sulfide-bearing superjacent bottom waters gradually overwhelms the light sulfide component.

Ore fluid and lead sources

The source of hydrothermal fluids and metals in the Anvil district is difficult to establish because of the limited amount of primary geologic and geochemical data available to assess the original ore-forming environment. However, the stratigraphic package hypothesized to underlie the Anvil Range provides an attractive reservoir within which subsurface waters could evolve into hot, metalliferous fluids. Subsurface waters in this reservoir could have leached evaporites and gained salinity for metal chloride complexing while gradually becoming geothermally heated. Interaction with coarse clastic reservoir rocks might have allowed metal solubilization from such sources as feldspar grains, pigmenting agents of red beds (Carpenter, 1979; Lentini and Shanks, 1983), or interbedded shales (Bischoff et al., 1981; Berndt, 1983).

During extensional tectonism in the Early Cambrian, the shale cap (Mt. Mye unit) may have been breached, allowing ore fluids to escape upward to the

sea floor. Volcanism may have been entirely passive, simply reflecting the tectonic environment. Alternatively, mafic igneous rocks may have had a more active role in transferring heat and perhaps some sulfide and metals to the ore fluid. In this regard, the Anvil Range deposits are notably richer in iron sulfides, and perhaps in copper-bearing sulfides, than other Selwyn basin lead-zinc deposits.

Lead isotopes are a useful indicator of the source of the lead in the fluids which formed the Anvil Range deposits. The Anvil deposits have a modest range of lead isotope ratios which form elongate fields on $^{207}Pb/^{204}Pb$-$^{206}Pb/^{204}Pb$ and $^{207}Pb/^{204}Pb$-$^{206}Pb/^{204}Pb$ diagrams (Figs. 13 and 14). The average lead isotope ratio growth curves of Godwin and Sinclair (1982) for shale-hosted deposits in the Canadian cordillera are shown for comparison. The curves are based on a three-stage model, the first two stages of which correspond to the Stacey and Kramers (1975) model. The third stage begins at 1.89 b.y. and the leads evolve until the time of mineralization in an environment which has constant $^{238}U/^{204}Pb = 12.16$ and $^{232}Th/^{204}Pb = 49.09$. The average evolution curves are useful for dating Selwyn basin shale-hosted deposits over a 200-m.y.-age range; these results imply an isotopically restricted lead source for all of the studied deposits. Godwin and Sinclair (1982) suggest that the source of the lead is sediment derived from Hudsonian basement of the Churchill province of the Canadian Shield. The isotopic compositions of the lead in the shale-hosted deposits are similar to the upper crustal leads contributed to the orogene, as defined by the plumbotectonics model of Doe and Zartman (1979).

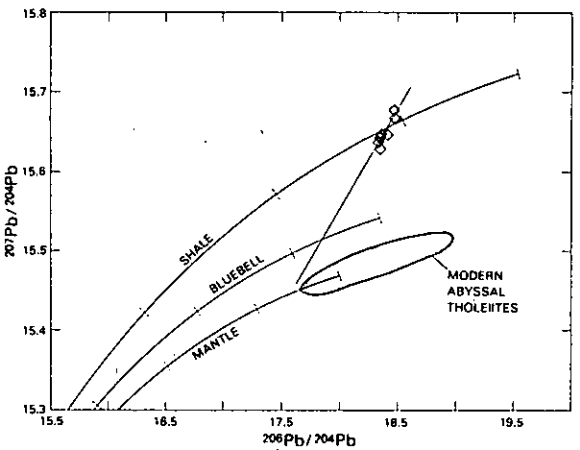

FIG. 13. Averaged lead isotope data for Anvil range deposits. Shale growth curve of Godwin and Sinclair (1982), the Bluebell growth curve of Andrew et al. (1984), the mantle evolution curve of Zartman and Doe (1981), and the field for modern abyssal tholeiites from Tatsumoto (1978) are shown for comparison. The averaged data plot along a regression line with a slope of 0.25 and $r^2 = 0.84$, which suggests a two-component source consisting of leads evolved along the shale curve with minor mantle contribution.

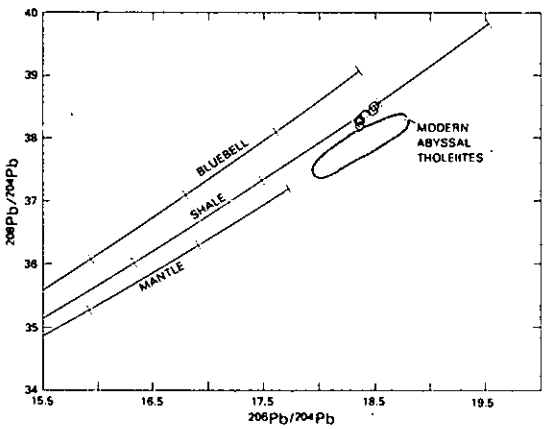

FIG. 14. Averaged lead isotope data for Anvil range deposits. Shale growth curve of Godwin and Sinclair (1982), the Bluebell growth curve of Andrew et al. (1984), the mantle evolution curve of Zartman and Doe (1981), and the field for modern abyssal tholeiites from Tatsumoto (1978) are shown for comparison. Data plot slightly below the shale curve which suggests that a lower crustal lead component such as that represented by the Bluebell curve is not represented.

Andrew et al. (1984) have developed an additional curve, called the Bluebell curve (Figs. 13 and 14), for evolution of lower crustal and/or mantle leads in the Omineca crystalline terrain of southeastern British Columbia. Interestingly, some deposits identified by Andrew et al. (1984) have leads which are intermediate between the two growth curves and plot along "mixing line isochrons," indicating synchronous lead extraction from the two source reservoirs at the time of deposit formation.

Average lead isotope ratio values for the individual Anvil deposits are tightly clustered near the shale curve on the $^{207}Pb/^{204}Pb$-$^{206}Pb/^{204}Pb$ diagram (Fig. 13), along a line with a slope of 0.25 ($r^2 = 0.84$). This line probably represents mixing of two or more lead components, and thus it may or may not have chronological significance. However, the regression line intersects the Bluebell growth curve at an age of about 0.30 b.y., hence a mixing line isochron is not indicated. Moreover, the Anvil data plot on the $^{208}Pb/^{204}Pb$-$^{206}Pb/^{204}Pb$ diagram slightly below the shale curve but considerably removed from the Bluebell curve (Fig. 14), which argues against a lower crustal lead component like that represented by the Bluebell curve. We speculate that the upper crustal leads of the Anvil deposits may contain a very minor mantle lead component derived from volcanics in the sedimentary sequence. The fields of modern abyssal tholeiites (Tatsumoto, 1978) and the plumbotectonic mantle evolution curves (Zartman and Doe, 1981) are shown for comparison in Figures 13 and 14, and are

consistent isotopically with the argument for a minor mantle component.

Additional information on the lead sources can be gained by examining the distributions of individual samples from each deposit on a $^{207}Pb/^{204}Pb$-$^{206}Pb/^{204}Pb$ plot (Fig. 15). The fields of data for each deposit tend to cluster in elongate bands which roughly parallel the regression line for the averaged data (Fig. 15). The lead isotope variability in the Anvil Range samples might be related to lead solubility in the hydrothermal fluid or to heterogeneity of sources. The more radiogenic components might have been preferentially leached from the uranium-rich fraction of the rock, removing lead from easily reached locations such as grain surfaces and microfractures where soluble uranium has previously existed (Doe et al., 1966). However, differential leaching tends to produce much flatter trajectories on the $^{207}Pb/^{204}Pb$-$^{206}Pb/^{204}Pb$ plot (Fehn et al., 1983). Alternatively, the source rocks may have been slightly heterogeneous with respect to lithology and lead isotope composition.

The lateral variation of $\delta^{34}S$ values within the DY deposit (Fig. 9) and the vertical increase of $\delta^{34}S$ values within the Faro deposit (Fig. 8) suggest that a small amount of the sulfide is derived from interaction with mafic igneous rocks, which may also provide some nonradiogenic lead. To test this hypothesis, $\delta^{34}S$ values were measured on splits of the DY deposit samples used for lead isotope studies, but no correlation is observed between sulfur and lead isotope ratio values (Table 6). However, as mentioned above, vertical variation in $\delta^{34}S$ values is not well developed in the DY deposit. Unfortunately, lead isotope ratio values were not determined on the samples from hole 66-52 from the Faro deposit, which show a systematic upward increase in $\delta^{34}S$ values. Nonetheless, it is interesting to note that the DY deposit has the least radiogenic lead isotope ratios of any of the Anvil range deposits and is the only deposit which contains substantial amounts of mafic meta-igneous rocks (Fig. 4b). If the postulated mantle lead component is derived from these rocks, then sulfur apparently was not mobilized with the lead.

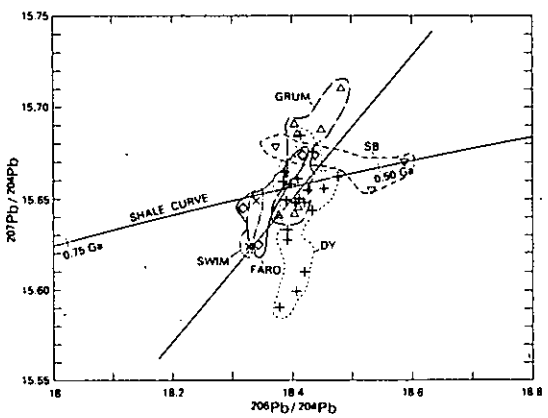

FIG. 15. Expanded plot of lead isotope data for individual samples from Anvil deposits. Regression (mixing) line from Figure 10 is shown for comparison. Data from several of the deposits fall in bands which parallel the mixing line.

In summary, the lead isotope ratio data indicate a fairly radiogenic upper crustal source for most of the lead. An excellent candidate for this source rock is the Proterozoic Grit unit (Gabrielse et al., 1973) which probably underlies the Mt. Mye unit in the Anvil area (Fig. 3). Intradeposit $\delta^{34}S$ variations (Figs. 8 and 9) and interdeposit lead isotope ratio variations (Fig. 15) suggest a possible small contribution (of Pb and S) from mafic igneous rocks, but much of the lead variability also can be attributed to heterogeneity of the upper crustal lead component.

Metallogenic Implications

Several important discoveries of major stratiform lead-zinc deposits recently have been made in the Selwyn basin (Carne and Cathro, 1982). Examples are Howards Pass with 525 million tons of 5 percent Zn and 2 percent Pb (Goodfellow, 1984), Cirque with at least 40 million tons of 7.8 percent Zn, 2.2 percent Pb, and 47 g/ton Ag (Jefferson et al., 1983) plus the other smaller deposits of the Gataga district (MacIntyre, 1983), the Tom and Jason deposits of the MacMillan Pass camp with approximately 26 million tons of 7 percent Zn and 6.8 percent Pb (Goodfellow, 1985), and of course the Anvil district with 92 million tons of 4.7 percent Zn, 3.6 percent Pb, and 50 g/ton Ag. Deposit age varies from Early Cambrian to Late Devonian and, even though all of these deposits fall into the "sedex" class, geologic setting, and host lithologies also vary widely. Clearly the Selwyn basin represents a major metallogenic province for Zn-Pb deposits. Why?

The results of the present study and of Goodfellow and Jonasson (1984) strongly implicate water column hydrogen sulfide, produced during periods of extreme anoxia and stagnation, as the principal source of sulfide in the ore deposits. The $\delta^{34}S$ values of sulfides in all the deposits are very heavy (Fig. 11), often approaching and even exceeding the values for contemporaneous seawater sulfate. Such values can only be attributed to reduction of a significant fraction of seawater sulfate in restricted subbasins. S/C ratios in unmineralized Anvil Range samples which greatly exceed values for modern marine sediments (Fig. 10) are further evidence for significant water column sulfide production. The Black Sea is a reasonable analog. In fact, the present Black Sea has almost exactly the same areal extent as the Selwyn basin presently preserved east of the Tintina fault. The Black Sea, however, has no known modern accumulations of Zn-Pb-

rich sediments, either because they do not exist or because of inadequate sea-floor exploration. Also, the present Black Sea water column is not experiencing the kind of quantitative sulfate reduction which must have occurred in the Selwyn basin.

The Selwyn basin apparently developed as a strongly reducing basin during much of its history, as evidenced by $\delta^{34}S$ values of diagenetic or sedimentary iron sulfides which generally exceed >10 per mil throughout the early Paleozoic history of the basin (Goodfellow and Jonasson, 1984). This is in marked contrast to modern bacteriogenic sulfides and sulfides from a number of ancient sedimentary sequences which often have $\delta^{34}S$ values in the −20 to −45 per mil range. However, in view of the Black Sea analogy, the long history of anoxia in the Selwyn basin clearly is not the only requirement for development of Zn-Pb deposits and a major metallogenic province. If so, then all anoxic basinal sequences would be expected to host such deposits. Many may, but clearly all do not.

An additional source of zinc and lead is probably required to turn an anoxic basin into a Zn-Pb province. In the case of the Anvil deposits, the $\delta^{34}S$ values of the baritic units and the lead isotope ratios of sulfides point to metalliferous brines derived from the underlying Proterozoic sequence. Decoupling of lead isotope ratios and $\delta^{34}S$ values in splits of the same samples further supports dual sources for the metals and the sulfides. Moreover, the fact that the Anvil deposits plot on a single lead isotope growth curve for a wide variety of stratiform and strata-bound Zn-Pb deposits from the Selwyn basin (Godwin and Sinclair, 1982) suggests that basinal brines may have been important metal suppliers to the basin over a considerable period of geologic time. Thus, the formation of a major metallogenic province for Zn-Pb, such as the Selwyn basin, requires the contemporaneous development of the following geologic framework: (1) an underlying or flanking sedimentary sequence capable of producing metalliferous brines, (2) a restricted anoxic marine basin, and (3) structural or stratigraphic pathways (with or without convective geothermal activity) to deliver basinal brine to anoxic bottom waters. Contemporaneous superimposition of these factors is probably not too unusual in the geologic record but the Grit unit is, perhaps, an unusually good source rock for metalliferous brines.

It is not inappropriate, in view of recently published hypotheses (Sawkins, 1984), to speculate on the driving mechanism of possible brine circulation from the Grit unit into the Selwyn basin. Badham (1981) clearly stated the case for a genetic relation between fluids produced by basin dewatering and shale-hosted lead-zinc deposits. Sawkins (1984) carried this idea a step further, and citing Cathles and Smith (1983), called upon episodic dewatering during basin compaction to produce multilayered stratiform Pb-Zn deposits. The Grum and DY deposits in the Anvil district are certainly excellent and representative examples of multilayered deposits. However, the lead isotope growth curve of Godwin and Sinclair (1982) is strong evidence for a constant lead source and evolution over a period of at least 200 m.y. If basin dewatering due to compaction is the driving mechanism, then fluids must be expelled downward from the accumulating pile of basinal sediments into the underlying Grit unit and then migrate laterally until structural pathways to the sea floor are encountered. Alternatively, Garven and Freeze (1984a, b) have recently developed a model whereby fluid flow is driven by gravity on a sloping water table related to topography flanking a basin. Such flow regimes may be stable for geologically long periods of time, as long as topography is not drastically altered by rapid erosion. This model also may be applicable to the Selwyn basin situation, where important deposits developed from Early Cambrian to Late Devonian, and significant land masses existed to the east, at least during part of this time period (Cecile, 1982).

The general similarity of Zn-Pb deposits in the Selwyn basin is striking, but in detail individual deposits differ considerably. The Howards Pass deposits are fine-grained, rhythmically banded intercalations of sulfides with limestones, carbonaceous mudstones, and cherty mudstones. Copper, silver, barium, and pyrite are relatively minor. No well-developed feeder or stringer zone is known and brecciation is relatively unimportant. The overwhelming impression is of slow accumulation of metallic sulfides over a long period of time.

In contrast, the Tom and Jason deposits at MacMillan Pass occur in turbidites and breccias related to syndepositional normal faults. Crosscutting stringer and alteration zones carry a significant portion of the mineralization (which includes important Ag and Cu) and barite is prominent, especially in upper zones. The Cirque deposit in the Cataga district is, perhaps, intermediate between the Howards Pass and MacMillan Pass deposits. The host rocks consist of thick-bedded, carbonaceous, siliceous shale, and locally, graded siliceous siltstone laminae. Occasional intraformational breccias occur. The deposit is baritic throughout and host-rock interlamination is rather uncommon. Cu or stringer mineralization are unknown, but deposit zonation points to a discrete source area. Ag content is significant.

The Anvil deposits contrast strikingly with the other Selwyn basin deposits described above. Principal differences relate to the rather high metamorphic grade, and more importantly, primary features such as very high iron sulfide content of the ore zones, fairly well defined sericitic alteration zones, well-developed ore facies zonation, and more abundant association of volcanic rocks. These differences strongly suggest higher temperature in the exhalative envi-

ronment of the Anvil Range, perhaps due to closer spatial association with volcanics and subvolcanic heat-generating plutons.

Thus, it appears that development of the Selwyn basin Zn-Pb province relates to the broad geologic framework and is a fairly normal consequence of the geotectonic development of the area. A metalliferous source rock and a long-lived hydrodynamic regime is required to deliver metalliferous brines to the basin. The long history of extreme anoxia in the basin provides a ready and ample sulfide source. Stratiform sulfides deposits form, rather slowly, due to mixing of pooled metalliferous brines with superjacent sulfidic seawater. Brine egress to the sea floor requires tectonic conduits. Fluid circulation may be simply gravity driven or may be aided by buoyancy effects due to subvolcanic plutons. Variations in deposit types are due to local variations in the rate and temperature of ore fluid venting and to variations in the local tectonic and lithologic framework.

Acknowledgments

This study was carried out at the Department of Geology and Geophysics, University of Wisconsin, Madison, Wisconsin, and the Geology-Geophysics Geochronology Laboratory, the University of British Columbia, Vancouver, B.C., with the generous support of the Cyprus-Anvil Mining Corporation.

We thank June Pounder for laboratory assistance and Robert Zierenberg for discussion of genetic models. Excellent reviews of early versions of the manuscript were provided by Bruce Doe, Robert Ayuso, Bob Criss, John Slack, Eric Force, Colin Godwin, Ian Jonasson, and Wayne Goodfellow. We thank Lee Pigage, Brian Hall, Darryl Hansen, and George Gorzinski for many helpful discussions and for logging much of the core. Particularly useful comments by Brian Skinner and Robert Ayuso served to focus the final version of the manuscript.

June 20, 1985; June 19, 1986

REFERENCES

Andrew, A., Godwin, C. I., and Sinclair, A. J., 1984, Mixing line isochrons: A new interpretation of galena lead isotope data from southeastern British Columbia: ECON. GEOL., v. 79, p. 919–932.

Badham, J. P. N., 1981, Shale-hosted Pb-Zn deposits: Products of exhalation of formation waters?: Inst. Mining Metallurgy Trans., v. 90, p. B70–B76.

Berndt, M., 1983, Experimental brine-mud interaction at 250°C and 500 bars: Unpub. M.S. Thesis, Univ. Wisconsin, 121 p.

Berner, R. A., 1964, Distribution and genesis of sulfur in some sediments from the Gulf of California: Marine Geology, v. 1, p. 117–140.

Bischoff, J. L., Radtke, A. S., and Rosenbauer, R. J., 1981, Hydrothermal alteration of graywacke by brine and seawater: Roles of alteration and chloride complexing on metal solubilization at 200°C and 350°C: ECON. GEOL., v. 76, p. 659–676.

Blount, C. W., 1977, Barite solubilities and thermodynamic quantities up to 300°C and 1400 bars: Am. Mineralogist, v. 62, p. 942–957.

Blusson, S. L., 1966, Frances Lake, Yukon Territory and District of Mackenzie: Canada Geol. Survey Map 8-1967.

Broecker, W. S., and Oversby, V. M., 1971, Chemical equilibria in the earth: New York, McGraw-Hill, 318 p.

Campbell, F. A., and Ethier, V. G., 1974, Sulfur isotopes, iron content of sphalerites, and ore textures in the Anvil ore body, Canada: ECON. GEOL., v. 69, p. 482–493.

Carne, R. C., and Cathro, R. J., 1982, Sedimentary exhalative (sedex) zinc-lead-silver deposits, northern Canadian Cordillera: Canadian Mining Metallurgy Bull., v. 75, no. 840, p. 66–78.

Carpenter, A. B., 1979, Interim report on lead and zinc in oilfield brines in the central gulf coast and in southern Michigan: Am. Inst. Mining Metall. Petroleum Engineers, Preprint 79-95, 15 p.

Cathles, L. M., and Smith, A. T., 1983, Thermal constraints on the formation of Mississippi Valley-type lead-zinc deposits and their implications for episodic basin dewatering and deposit genesis: ECON. GEOL., v. 78, p. 983–1002.

Cecile, M. P., 1982, The lower Paleozoic Misty Creek embayment, Selwyn basin, Yukon and Northwest Territories: Canada Geol. Survey Bull. 335.

Claypool, G. E., Holser, W. T., Kaplan, I. R., Sakai, H., and Zak, I., 1980, The age curves of sulfur and oxygen isotopes in marine sulfate and their mutual interpretation: Chem. Geology, v. 28, p. 199–260.

Cole, R. D., and Picard, M. D., 1981, Sulfur-isotope variations in marginal-lacustrine rocks of the Green River Formation, Colorado and Utah: Soc. Econ. Paleontologists Mineralogists Spec. Pub. 31, p. 261–275.

Deuser, W. G., 1974, Evolution of anoxic conditions in Black Sea during Holocene: Am. Assoc. Petroleum Geologists Mem. 20, p. 133–136.

Doe, B. R., Hedge, C. E., and White, D. E., 1966, Preliminary investigation of the source of lead and strontium in deep geothermal brines underlying the Salton Sea geothermal area: ECON. GEOL., v. 61, p. 462–483.

Doe, B. R., and Zartman, R. E., 1979, Plumbotectonics: The Phanerozoic, *in* Barnes, H. L., ed., Geochemistry of hydrothermal ore deposits: New York, Wiley Intersci., p. 22–70.

Eisbacher, G. H., 1980, Sedimentary tectonics and glacial record in the Windermere Supergroup, Mackenzie Mountains, Northwestern Canada: Canada Geol. Survey Paper 80-27, 40 p.

Emery, K. O., 1960, The sea off southern California: New York, Wiley, 366 p.

Fehn, U., Doe, B. R., and Delevaux, M. H., 1983, The distribution of lead isotopes and the origin of Kuroko ore deposits in the Hokuroku district, Japan: ECON. GEOL. MON. 5, p. 488–506.

Franklin, J. M., Lydon, J. W., and Sangster, D. F., 1981, Volcanic-associated massive sulfide deposits: ECON. GEOL. MON. 5, p. 485–627.

Gabrielse, H., Blusson, S. L., and Roddick, J. A., 1973, Geology of Flat River, Glacier Lake and Wrigley Lake map areas: Canada Geol. Survey Mem. 366, 153 p.

Gardner, H. D., and Hutcheon, I., 1985, Geochemistry, mineralogy, and geology of the Jason Pb-Zn deposits, Macmillan Pass, Yukon, Canada: ECON. GEOL., v. 80, p. 1257–1276.

Garven, G., and Freeze, R. A., 1984a, Theoretical analysis of the role of groundwater flow in the genesis of stratabound ore deposits. 1. Mathematical and numerical model: Am. Jour. Sci., v. 284, p. 1085–1124.

——— 1984b, Theoretical analysis of the role of groundwater flow in the genesis of stratabound ore deposits. 2. Quantitative results: Am. Jour. Sci., v. 284, p. 1125–1174.

Godwin, C. I., and Sinclair, A. J., 1982, Average lead isotope growth curves for shale-hosted zinc-lead deposits, Canadian Cordillera: ECON. GEOL., v. 77, p. 675–690.

Goldhaber, M. B., and Kaplan, I. R., 1974, The sedimentary sulfur cycle: The Sea, *in* Goldberg, E. D., ed., Marine chemistry: New York, Wiley-Intersci., p. 569–655.

Goodfellow, W. D., 1984, Geochemistry of rocks hosting the Howards Pass (XY) strata-bound Zn-Pb deposit, Selwyn basin,

Yukon Territory, Canada, *in* Janelidze, T. V., and Tvalchrelidze, A. G., eds., Proceedings of the sixth quadrennial IAGOD Symposium held in Tbilisi, USSR, September 6–12, 1982: Stuttgart, E. Schweizerbart'sche, p. 91–112.

—— 1985, Geochemistry unveils 'blind' deposits: GEOS [Ottawa, Canada], v. 14, p. 17–20.

Goodfellow, W. D., and Jonasson, I. R., 1984, Ocean stagnation and ventilation defined by ^{34}S secular trends in pyrite and barite, Selwyn basin, Yukon: Geology, v. 12, p. 583–586.

—— 1986, Environment of formation of the Howards Pass (XY)Zn-Pb deposit, Selwyn basin, Yukon: Canadian Inst. Mining Metallurgy Spec. Vol., Mineral Deposits of the Northern Cordillera, in press.

Gordey, S. P., 1978, Stratigraphy and structure of the Summit Lake area, Yukon and Northwest Territories: Canada Geol. Survey Paper 78-1A, p. 43–48.

Gustafson, L. B., and Williams, N., 1981, Sediment-hosted stratiform deposits of copper, lead, and zinc: ECON. GEOL. 75TH ANNIV. VOL., p. 139–178.

Hartmann, V. M., 1973, Untersuchung von suspendiertem material in den hydrothermallangen des Atlantis II-Tiefs: Geol. Rundschau, v. 62, p. 742–754.

Hartmann, V. M., and Nielsen, H., 1969, S^{34} werte in rezente meeressedimenten und ihre deutung am beispiel einiger sedimentprofile aus der westlichen ostsee: Geol. Rundschau, v. 58, p. 621–655.

Holland, H. D., and Malinin, S. D., 1979, The solubility and occurrence of non-ore minerals, *in* Barnes, H. L., ed., Geochemistry of hydrothermal ore deposits: New York, Wiley Intersci., p. 461–508.

Jennings, D. S., and Jilson, G. A., 1986, Geology and sulfide deposits of Anvil range, Yukon Territory: Canadian Inst. Mining Metallurgy., Spec. Vol., Mineral Deposits of the Northern Cordillera, in press.

Jennings, D. S., Jilson, G. A., and Pigage, L. C., 1980, Anvil Range stratigraphy, south-central Yukon Territory [abs.]: Geol. Assoc. Canada, Cordilleran Sec., Programme and Abstracts, January 1980, p. 16–17.

Jefferson, C. W., Kilby, D. B., Pigage, L. C., and Roberts, W. J., 1983, The Cirque barite-zinc-lead deposits, northeastern British Columbia: Toronto, Mineralog. Assoc. Canada, Short Course Handbook, v. 8, p. 121–140.

Jorgensen, B. B., 1979, A theoretical model of the stable sulfur isotope distribution in marine sediments: Geochim. et Cosmochim. Acta, v. 43, p. 363–374.

Kaplan, I. R., 1975, Stable isotopes as a guide to biogeochemical processes: Royal Soc. [London] Proc., sec. B, v. 189, p. 183–211.

Kuo, S. L., 1976, Geology and geochemistry of stratabound ore deposits in south-central Yukon Territory and southwestern District of Mackenzie, Northwest Territories: Unpub. Ph.D. dissert., Univ. Alberta, 597 p.

Kuo, S. L., and Folinsbee, R. E., 1974, Lead isotope geology of mineral deposits spatially related to the Tintina trench, Yukon Territory: ECON. GEOL., v. 69, p. 806–813.

Large, D., 1980, Geological parameters associated with sediment-hosted, submarine exhalative Pb-Zn deposits: Geol. Jahrb., ser. D, no. 40, p. 49–129.

LeCouter, P. C., 1973, A study of lead isotopes from mineral deposits in southeastern British Columbia and in the Anvil Range, Yukon Territory: Unpub. Ph.D. dissert., Univ. British Columbia, 142 p.

Lentini, M. R., and Shanks, W. C., III, 1983, Experimental study of brine-arkose interaction at 200°C and 500 bars: Origin of metalliferous oil field brines and Mississippi Valley type ore deposits, *in* Kisvarsanyi, G., Grant, S. K., Pratt, W. P., and Koenig, J. W., eds., International conference on Mississippi Valley type lead-zinc deposits. Proceedings volume: Rolla, Univ. Missouri-Rolla Press, p. 195–205.

Leventhal, J. S., 1983, An interpretation of carbon and sulfur relationships in Black Sea sediments as indicators of environments of deposition: Geochim. et Cosmochima. Acta, v. 47, p. 133–137.

MacIntyre, D. G., 1983, Geology and stratiform barite-sulphide deposits of the Cataga district, northeast British Columbia: Toronto, Mineralog. Assoc. Canada, Short Course Handbook, v. 8, p. 85–120.

Mako, D. A., and Shanks, W. C., III, 1984, Stratiform sulfide and barite-fluorite mineralization of the Vulcan prospect, Northwest Territories: Exhalation of basinal brines along a faulted continental margin: Canadian Jour. Earth Sci., v. 21, p. 78–91.

Migdisov, A. A., Cherkovskiy, S. L., and Grinenko, V. A., 1974, The effects of formation conditions on the sulfur isotopes of aquatic sediments: Geochemistry Internat., v. 11, p. 1028–1047.

Modene, J. S., 1982, Origin and sulfur isotope geochemistry of the Crum deposit, Anvil Range, Yukon Territory, Canada: Unpub. M.S. thesis, Univ. Wisconsin, 158 p.

Monger, J. W. H., and Price, R. A., 1979, Geodynamic evolution of the Canadian Cordillera—progress and problems: Canadian Jour. Earth Sci., v. 16, p. 770–791.

Pigage, L. C., and Anderson, R. G., 1985, The Anvil plutonic suite, Faro, Yukon Territory: Canadian Jour. Earth Sci., v. 22, p. 1204–1216.

Rees, C. E., 1978, Sulphur isotope measurements using SO_2 and SF_6: Geochim. et Cosmochim. Acta, v. 42, p. 383–390.

Ross, D. A., and Degens, E. T., 1974, The Black Sea: Am. Assoc. Petroleum Geologists Mem. 20, 593 p.

Sawkins, F. J., 1984, Ore genesis by episodic dewatering of sedimentary basins: Applications to giant Proterozoic lead-zinc deposits: Geology, v. 12, p. 451–454.

Shanks, W. C., III, and Bischoff, J. L., 1980, Geochemistry, sulfur isotope composition, and accumulation rates of Red Sea geothermal deposits: ECON. GEOL., v. 75, p. 445–459.

Shanks, W. C., III, Bischoff, J. L., and Kaplan, I. R., 1973, Sulfur isotope studies of evaporites and shales from sites 225, 227, and 228 in the Red Sea: Deep Sea Drilling Proj., Initial Repts., v. 23, p. 947–950.

Schwarcz, H. P., and Burnie, S. W., 1973, Influence of sedimentary environments on sulfur isotope ratios in clastic rocks—a review: Mineralium Deposita, v. 8, p. 264–277.

Stacey, J. S., and Kramers, J. D., 1975, Approximation of terrestrial lead isotope evolution by a two-stage model: Earth Planet. Sci. Letters, v. 26, p. 207–221.

Sweeney, R. E., and Kaplan, I. R., 1980, Stable isotope composition of dissolved sulfate and hydrogen sulfide in the Black Sea: Marine Chemistry, v. 9, p. 145–152.

Tatsumoto, M., 1978, Isotopic composition of lead in oceanic basalt and its implication to mantle evolution: Earth Planet. Sci. Letters, v. 38, p. 63–87.

Tempelman-Kluit, D. J., 1970a, Stratigraphy and structure of the "Keno Hill Quartzite" in Tombstone River map areas, Yukon Territory: Canada Geol. Survey Bull. 180, 102 p.

—— 1970b, The relationship between sulfide grain size and metamorphic grade of host rocks in some strata-bound pyritic ores: Canadian Jour. Earth Sci., v. 7, p. 1339–1345.

—— 1972, Geology and origin of the Faro, Vangorda, and Swim concordant zinc-lead deposits, central Yukon Territory: Canada Geol. Survey Bull. 208, 73 p.

—— 1979, Transported cataclasite, ophiolite and granodiorite in Yukon: Evidence of arc-continent collision: Canada Geol. Survey Paper 79-14, 27 p.

Vinogradov, A. P., Grinenko, V. A., and Ustinov, V. I., 1962, Isotopic composition of sulfur compounds in the Black Sea: Geochemistry Internat., v. 10, p. 973–997.

Williams, N., 1978, Studies of the base metal sulfide deposits at McArthur River, Northern Territory, Australia: II. The sulfide-S and organic-C relationships of the concordant deposits and their significance: ECON. GEOL., v. 73, p. 1036–1056.

Zartman, R. E., and Doe, B. R., 1981, Plumbotectonics—the model: Tectonophysics, v. 75, p. 135–162.